Coordination Chemistry Reviews 320-321 (2016) 82–99

Contents lists available at ScienceDirect

Coordination Chemistry Reviews

journal homepage: www.elsevier.com/locate/ccr

Supported binary hybrid nanomaterials and their applications

Nafiseh Moghimi, F.R. Rahsepar, K.T. Leung

WATLab, and Department of Chemistry, University of Waterloo, Waterloo, Ontario N2L 3G1, Canada

Contents

ARTICLE INFO

Article history:
Received 21 December 2015
Received in revised form 16 April 2016
Accepted 17 April 2016
Available online 22 April 2016

Keywords:
Hybrid materials
Supported nanostructures
Catalysts
Chemical sensing
Green energy
Nanotechnology

ABSTRACT

Hybrid nanostructured materials provide new functionalities not found in their individual pristine nanocomponents. The present review focuses on successful extension from single-component materials to different hybrid nanostructured materials and on their novel applications in chemical sensing, green energy, and advanced manufacturing. Hybridization is performed mainly by electrochemical deposition and a number of advanced dry deposition techniques, including pulsed laser deposition and size-selected magnetron sputtering. Hybrid nanostructured materials are classified into two main categories: A + B systems consisting of two materials of different chemical identities including metal–metal, metal–metal oxide, metal–biomolecule, and metal oxide–metal oxide; and A + A′ systems consisting of one material but with two components of different crystalline phases, with and without dopants, and with and without defects. The novelties and synergistic properties of these hybrid nanomaterials are exploited for the development of emerging applications.

* Corresponding author. Tel.: +15198884567 x35826; fax: +15197460435.
E-mail address: tong@uwaterloo.ca (K.T. Leung).

http://dx.doi.org/10.1016/j.ccr.2016.04.011
0010-8545/

1. Hybrid nanostructures

Nanotechnology has attracted a lot of recent attention [1], because of its potential applications in catalysis [2,3], information and data storage [4–6], biotechnology and medicine [7], environment and energy [8], and advanced optics and electronics [9,10]. Its impact on our daily life is manifested by increasing commercialization of a wide variety of nanomaterials, especially nanoparticles (NPs), in cosmetic and heath products, green energy, storage media, and electronics. Nanostructured materials are especially interesting because they constitute a new type of materials with nanoscale properties that are very different from those of individual atoms and molecules and of bulk matter. Nanostructured materials have a much larger surface area to volume ratio (or specific surface area) than their bulk counterpart, which along with their quantum size effects forms the basis for their unique physicochemical nanoscale properties.

Hybrid nanostructured materials constructed from more than one component have also attracted increased interest due to their additional functionalities [11–14]. The term "hybrid nanostructure" is commonly used to describe a discrete multi-component nanostructure, which includes multi-metallic systems and alloy NPs [10]. These components could be two (or more) metals, or a metal and an organic or bio-molecule, or a metal and an inorganic material such as a metal oxide. There are a number of important incentives to combine two or more components together to make a composite nanostructure. For instance, the surface chemical properties of a particle can be modified by coating with a second material to improve its colloidal stability or resistance to oxidation [10]. New synergetic effects can be created upon alloy formation of two metals. Additional functionality may also be introduced to a nanostructure for bio-applications, for instance, by attaching an antibody for biological targeting application. There are many different plausible types and morphologies of hybrid nanostructures, with some of the key nanostructures shown schematically in Fig. 1 [10].

Hybrid materials can be divided into two main categories. Type A + B corresponds to two chemically different materials combined together, with each keeping its own chemical identity (formula). Type A + A′ refers to the combination of two components with the same chemical identity but different intrinsic properties (e.g., crystalline phases, amounts or types of defects, or both) or extrinsic properties (e.g., dopants). If the same shape is maintained, the hybrid material can be further divided into core-shell or mixed alloy nanostructures. The core-shell nanostructures could be made up of metal and metal, metal and semiconductor, metal and dielectric, or any other combinations. The order of the core and shell arrangement (e.g., semiconductor core metal shell vs metal core semiconductor shell) could also lead to radically different hybrid core-shell materials. There are even more variations in the different combinations of three materials (A, B, C) into outer shell A, inner shell B, and core C, all of which could exhibit different properties. There are many good literature reviews about bimetallic nanostructures and their properties [15–17]. The mixed alloy nanostructured materials are usually combinations of two metals, while combinations of a metal and a non-metal such as a metal oxide or a biomolecule, e.g. Fe–glucose oxidase hybridization, are also possible [18]. For hybrid materials that are made up of materials with two different shapes, there are also many possible combinations involving, e.g., spherical nanoparticles on wires, rods, walls, and nanoparticles with different shapes. We first consider type A + B materials consisting of two chemically different A and B materials with the same or different shapes, and provide a few examples of typical combinations along with their unique properties. This will then be followed by our discussion on type A + A′ materials.

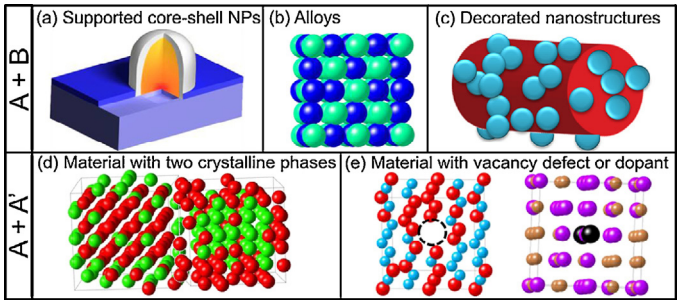

Fig. 1. Examples of common hybrid nanomaterials. Top panel (A + B): (a) Core-shell nanoparticles (NPs), (b) alloy metals, and (c) nanowires or nanorods decorated with metal nanoparticles. Bottom panel (A + A'): (d) Alloy metals with the same composition but different crystalline phases, and (e) metal oxides with vacancy defects (left) or dopants (right).

2. Type A + B materials: binary hybrid materials with two chemically different components

2.1. Metal–metal

Bimetallic NPs belong to a unique class of materials that shows a combination of sometimes very different properties associated with two constituent metals. In many cases, their specific physical and chemical properties are greatly enhanced owing to synergistic effects [19,20]. Based on the mixing pattern, bimetallic NPs can be divided into three main types [9]:

(a) Core-shell alloy NPs (Fig. 2a) consist of a core of one type of material (A) surrounded by a shell of another type of material (B), with possible mixing between the core and the shell materials at their interface.
(b) Segregated alloy NPs or heterostructures [1] (Fig. 2b) consist of segregated A and B clusters or domains, which may share a

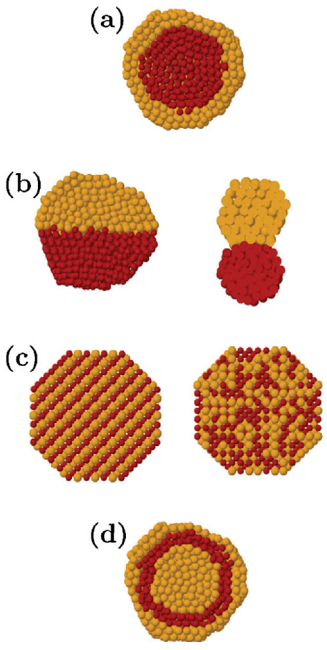

Fig. 2. Schematic representations of three main types of bimetallic nanoparticles of possible mixing patterns: (a) core-shell, (b) segregated, and (c) mixed alloy systems, plus more complex bimetallic systems such as (d) three-shell alloy system.
Reprinted with permission from: R. Ferrando, J. Jellinek, and R.L. Johnston, Chem. Rev. 108 (2008) 845–910. Copyright (2008) by the American Chemical Society.

mixed interface (left) or may only have a small number of A–B bonds (right).

(c) Mixed A–B alloy NPs (Fig. 2c) could be either ordered (left) or randomly mixed (i.e., a solid solution, right). As the more common type of alloy NPs, randomly mixed alloy NPs are what have often been referred to as "alloy" NPs in the literature. These alloy NPs with the intermixed coordination can be found in a wide variety of systems [9].

In addition to these three main types of bimetallic NPs, multi-shell alloy NPs (Fig. 2d) containing layered or onion-like alternating –A–B–A– shells are also possible. Metastable structures of this type have been suggested for the growth of Cu—Ag, Ni—Ag, and Pd—Ag NPs in computer simulation studies [21–23]. Bimetallic alloy NPs (A_mB_n, with m and n integers) can be generated with a variety of controlled size (m + n) and relative composition or stoichiometry (m/n).

Among all the bimetallic NPs, bimetallic mixed alloy and core-shell NPs are the most popular nanomaterials because of their important applications in catalytic reforming reactions, pollution control, alcohol oxidation, and numerous other catalytic reactions [24–29]. These NPs exhibit a prominent characteristic increase in solid solubility of the alloy components with decreasing particle size. The "alloy" properties of these NPs are found to depend not only on their relative compositions and crystal structures, but also on their sizes and shapes [30]. Alloy NPs can be synthesized in a variety of media, including as-born in NP beams, growth in colloidal solutions, and immobilized on surfaces or inside pores. These alloy NPs are particularly interesting because their chemical and physical properties can be tuned by controlling the composition and atomic ordering as well as the size and shape of the NPs. Indeed, alloy NPs could display not only magic-number sizes but also magic compositions, i.e., compositions at which the alloy NPs exhibit special stability and/or other enhanced properties [9].

Alloy NPs may also be classified as "free"/"bare" or "passivated"/"coated", depending on whether the surface of the NP is stabilized by surfactant molecules or ligands [9]. Free NPs are usually produced in a molecular beam or the gas phase, while passivated NPs can be generated in both the solution and gas phases. Alloy NPs may also be "supported" on surfaces or inside porous materials. One challenge in studying bare metal NPs is that it could be difficult to isolate and handle them. To enable the investigation of near-uniformly sized NPs and to exploit NP properties in device applications, it is often necessary to protect them individually with a shell. NPs can also be deposited from a solution onto a (conductive) substrate or from the gas phase onto a substrate such as graphite, silicon, or an inorganic oxide. For applications in which the NPs need to be immobilized on a surface (e.g. sensing), synthesis methods for supported NPs are more appropriate.

A variety of methods can be used for making bimetallic NPs, and they include chemical reduction [10,13,31–33], galvanic replacement [34,35], template growth [36–38], radiolysis and sonochemical synthesis [9,39–41], molecular beams and ion implantation [9,42–46], and electrochemical synthesis [47–49]. We focus on the electrochemical synthesis method for metal–metal hybridization because of the many advantages of this method over other methods. For instance, wet chemical methods conducted at room temperature have been used to produce amorphous alloy NPs [50], while inorganic salts can be reduced to produce crystalline NPs in both aqueous and non-aqueous media [51]. It is, however, very difficult to obtain a narrow size distribution of NPs with these methods near room temperature, making it necessary to conduct the synthesis at a higher temperature (above 300 °C) and often in the presence of surfactants [52]. Although surfactants are often used to stabilize the dispersion of NPs and to prevent their aggregation, incorporation of bulky or strongly binding surfactants into the NPs can affect their properties, sometimes in an undesirable way. Dry synthesis methods, such as arc discharge [53] and hydrogen plasma reaction [54], can produce spherical NPs or powders. However, the products so obtained often agglomerate into aggregates of NPs or chains especially for magnetic particles. This makes the generation and study of uniformly dispersed, individually separated NPs challenging.

Electrochemical methods have the advantage of producing NPs with a uniform spatial distribution without agglomeration on the substrate, which therefore provides the maximum exposed surface for electro-catalysis without additional steps. Electrodeposition usually results in highly crystalline NPs with a very thin oxide shell that is formed in-situ in the synthesis. This oxide shell can sometimes serve as a protective layer to insulate the core from further oxidation, therefore making the hybrid NPs stable in air. Electrodeposition can also be performed in a mild solution (close to neutral pH) at room or low temperature (4 °C), which is highly desirable for hybridization of metals with biomolecules. For sensor applications that require supported NPs, the electrochemical method does not require additional steps for electrode preparation. Using the electrochemical deposition method, we obtain a series of Fe-based and Au-based bimetallic alloy NPs, including FeM (M = Ni, Pt, Au, Pd) and AuM (M = Ni, Pt).

2.1.1. FeNi

Driven by the increasing need for low-cost soft magnets [55,56], catalysts [57], and biosensors [58], the study of bimetallic and trimetallic Fe-based nanoparticles (e.g., FeNi, FeCo, FeCoNi, FeNiZn) is of paramount importance to these and other emerging applications. Not only can the relative compositions and crystal structures of these nanoalloys define the "alloy" properties, their sizes and shapes can also play an important role [30]. As one of the most widely used magnetic materials, FeNi alloys, particularly in the form of spherical NPs over a wide size range (10–500 nm), have been synthesized by a variety of methods. In most of these synthesis methods, the control on shape and size of these alloy NPs is made possible only by using high temperature or surfactants. Since these NPs are inherently magnetic, uniform spatial distribution of well-dispersed NPs is a special challenge because of their propensity for agglomeration and chain formation.

We use electrochemical deposition because it is a facile, surfactant-free and single-step technique, and it enables us to synthesize air-stable FeNi alloy NPs, with narrow size distributions and different shapes, that are uniformly dispersed on a Si substrate. All the synthesis can also be carried out at room temperature [59]. We further demonstrate that the shape of these NPs evolves from Fe-rich concave cubes to Ni-rich truncated spheres and this shape evolution can be correlated with their phase transformation from bcc to fcc. Using this co-electrodeposition method with boric acid as the supporting electrolyte, the surfaces of the NPs are passivated in the solution because of in-situ formation of Ni-doped Fe oxides on top of the NPs. This surface passivation prevents further oxidation in air and results in the remarkable air stability observed for these NPs. Fig. 3 compares the scanning electron microscopy (SEM) images of pristine Fe and Ni NPs, with those of FeNi alloy NPs prepared by co-electrodeposition. Evidently, well-dispersed cubic Fe NPs are obtained together with bigger NP clusters, and they lead to a broad size distribution. This suggests that Fe NPs follow progressive nucleation in the growth mechanism. By introducing Ni^{2+} as a second component into the Fe^{2+} solution, the nucleation changes from a progressive to instantaneous mechanism, which results in more uniform deposition and a narrower size distribution for FeNi NPs [59].

Fig. 4 shows the high-magnification SEM images, transmission electron microscopy (TEM) energy dispersive X-ray analysis (EDX) line scans and schematic models of the FeNi NPs. The EDX line scan

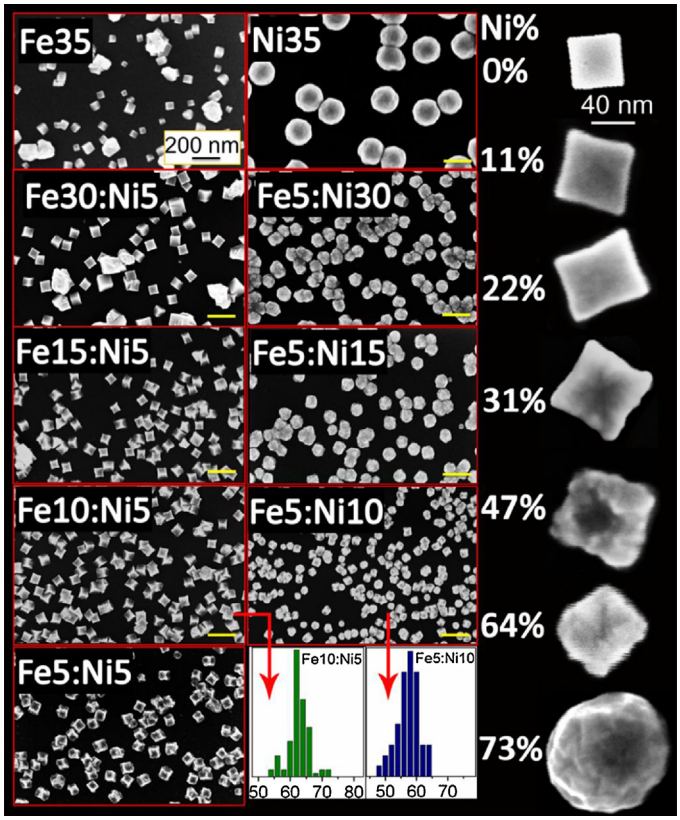

Fig. 3. SEM images of FeNi alloy nanoparticles electrodeposited on a hydrogen-terminated Si(100) substrate at −1.4 V (vs Ag/AgCl) for 20 s in different FeX:NiY solutions, where X and Y correspond to the concentrations in mM of $FeCl_2$ and $NiCl_2$, respectively. Center bottom panel presents the corresponding particle size distributions for Fe10:Ni5 and Fe5:Ni10. Right panel shows the high-magnification SEM images of FeNi alloy NPs for Ni at. % (as determined by energy dispersive X-ray analysis) of 0% (Fe35), 11% (Fe30:Ni5), 22% (Fe15:Ni5), 31% (Fe10:Ni5), 47% (Fe5:Ni5), 64% (Fe5:Ni10), and 73% (Fe5:Ni15).

Reprinted with permission from: N. Moghimi, S. Bazargan, D. Pradhan, K.T. Leung, J. Phys. Chem. C 117 (2013) 4852–4858. Copyright (2013) by the American Chemical Society.

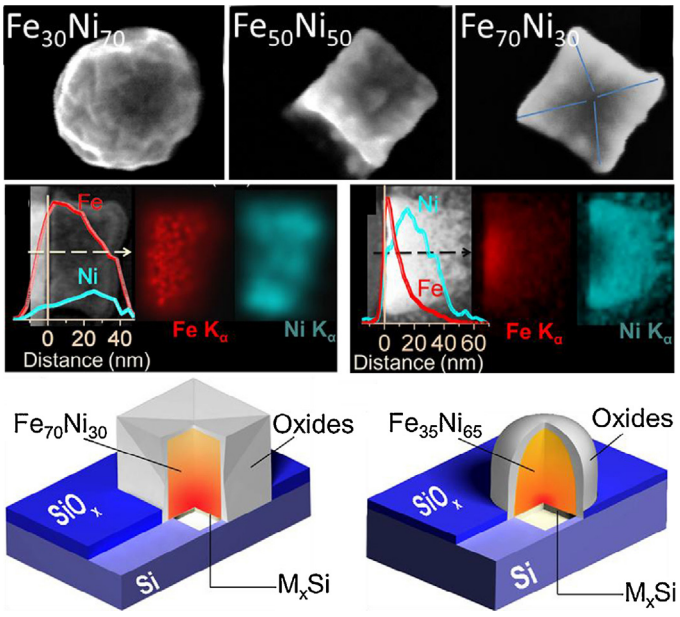

Fig. 4. Top panel: High-magnification SEM images of Fe_xNi_y alloy with different Ni contents, where x and y are relative at. % of Fe and Ni, respectively. The average sizes are 93 nm for $Fe_{30}Ni_{70}$, 62 nm for $Fe_{50}Ni_{50}$ and 63 nm for $Fe_{70}Ni_{30}$. Middle panel: EDX line scans and EDX-TEM mapping of a typical concave nanocube and a nanosphere. Bottom panel: Schematic models of a $Fe_{70}Ni_{30}$ nanocube and a $Fe_{35}Ni_{65}$ nanosphere, as inferred from depth-profiling X-ray photoelectron spectroscopy and TEM data. Both Fe_xNi_y alloy cores are also covered individually by an oxide shell (consisting of Ni-doped FeOOH and $NiFe_2O_4$) and supported on the Si substrate with a metal silicide (M_xSi) interface.

Reprinted with permission from: N. Moghimi, S. Bazargan, D. Pradhan, K.T. Leung, J. Phys. Chem. C 117 (2013) 4852–4858. Copyright (2013) by the American Chemical Society.

of oxygen and XPS analysis (data shown in the original article [59]) confirm the presence of a protective oxide layer on the shell of FeNi NPs. Indeed, these oxide layers prevent further oxidation and keep the NPs air-stable. In the synthesis and applications of magnetic metals (Fe-based materials), air stability is one of the greatest challenges. In the nano-size regime, air stability has become even more serious because the metallic NPs have a great affinity for oxygen and they immediately oxidize in air even at room temperature. This further complicates the synthesis methods with the need for an additional surface passivation step that often includes coating with metal oxides [60,61] or encapsulation in polymers [62], carbon nanotubes [63] and silica shells [64]. The present electrochemical approach therefore provides in-situ an oxide layer that greatly simplifies the synthesis of air-stable NPs.

We also study the shape-dependent properties of FeNi NPs, especially those with a rare concave cubic shape with high-index facets that could be obtained in different atomic percentages of Ni in FeNi alloy NPs. Concave cubes (cubes with high index planes) are especially rare, because cuboid nanostructures are usually enclosed by the {100} and {110} facets. We demonstrate that it is possible to produce FeNi concave nanocubes with the electrochemical deposition method by manipulating the growth kinetics involving a bimetallic system [65]. By taking advantage of highly reactive facets, we also develop a new approach for synthesizing concave nanocages by preferential etching in the center of concave cube through an electroleaching process. As a model for evaluating chemical sensing reaction, electro-oxidation of 4-aminophenol is used to access the sensing performance of both concave nanocubes and nanocages. 4-Aminophenol is an important organic compound because it can be used for *Escherichia coli* detection and as an intermediate or degradation product in the synthesis of paracetamol in the pharmaceutical industry. Fig. 5 shows the SEM images of the concave nanocages obtained after 1, 2 and 3 cyclic voltammetric etching cycles. As expected, material dissolution starts at the centers of the concave faces, because of the highest strain and therefore highest chemical potential at these locations [66]. Leaching continues to the edges until the center of the nanocube is completely hollowed out. Detection of 4-aminophenol can be achieved by running cyclic voltammetry using the supported FeNi nanostructures as the catalysts. These sensing experiments show that concave nanocubes exhibit much better signal than octahedrons while nanocages exhibit even better signal than concave nanocubes. The concave nanocages obtained after the first cyclic voltammetric etching cycle show over a 10-fold enhancement in the current density measured at 0.45 V relative to the concave nanocubes and over a 100-fold enhancement when compared to the cuboctahedrons [65]. This demonstrates the remarkable catalytic reactivity obtained from these novel FeNi nanocages.

2.1.2. FePt, FePd and FeAu

Screening for high-performance catalysts with both high activity and selectivity is an essential part of the design and development of novel catalysts and sensors. Metallic NPs, especially noble metal NPs, are ideal catalysts for analytes with slow redox processes because they provide a large electrochemically active surface area

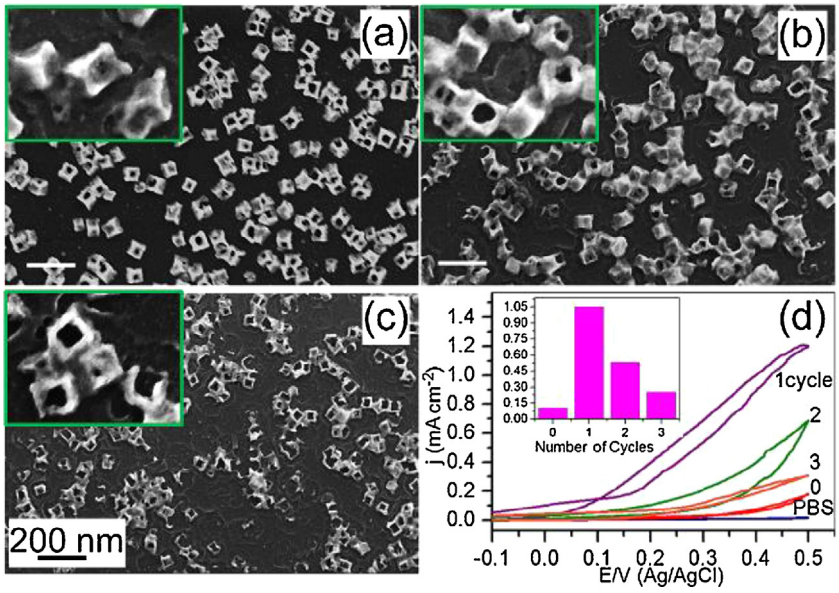

Fig. 5. (a–c) SEM images of FeNi nanocages obtained by 1, 2, and 3 cyclic voltammetric (CV) etching cycles in a 10 mM phosphate buffer solution (PBS) with pH 3 and a scan rate of 50 mV s^{-1}, (d) CV curves of concave nanocubes, obtained without and with the aforementioned 1, 2, and 3 etching cycles, in 5 mM 4-aminophenol in PBS (pH = 7). Inset shows the corresponding current densities measured at 0.45 V (vs Ag/AgCl) for these concave nanocubes obtained with different numbers of etching cycles.

Reprinted with permission from: N. Moghimi, M. Abd-Ellah, J.P. Thomas, M. Mohapatra, K.T. Leung, J. Am. Chem. Soc. 135 (2013) 10958–10961. Copyright (2013) by the American Chemical Society.

[67,68]. Of the noble metal catalysts, Pt NPs have been extensively used in the enhancement of electrochemical sensing for a variety of biomolecules [69], including glucose [70,71], DNA [72], and cholesterol [73]. The desire to design new lower-cost catalysts with minimal Pt content has led researchers to combine Pt with other less precious metal components [74–76]. We have electrochemically deposited FePt alloy NPs of different Pt contents (near the optimal value found for catalyst applications, i.e. 60–80%) directly on the surfaces of Si substrates and used them as electrodes for detection of ascorbic acid (i.e., vitamin C) [77]. We evaluate the results obtained with these alloy NPs, along with those found for pristine Pt NPs. Fig. 6a compares the cyclic voltammograms acquired at a sweep rate of 50 mV s^{-1} in a solution of 10 mM phosphate buffer solution with and without 1 mM ascorbic acid using a bare Si electrode and electrodes electrodeposited with pristine Fe NPs, pristine Pt NPs and $Fe_{30}Pt_{70}$ alloy NPs. While the bare Si electrode and Fe-NP electrode do not exhibit any current response in the presence of ascorbic acid, the Pt-NP electrode shows a discernibly stronger anodic response. However, the Pt-NP response is much weaker when compared to the alloy-NP electrode. For the alloy-NP electrode, the highest anodic peak current density (at +0.54 V vs Ag/AgCl) is found for the $Fe_{30}Pt_{70}$-NP electrode (where x and y in Fe_xPt_y correspond to relative atomic percentages of Fe and Pt in the alloy, respectively), with the anodic response following the trend: $Fe_{30}Pt_{70}$ > $Fe_{25}Pt_{75}$ > $Fe_{35}Pt_{65}$ > Pt > Fe (Fig. 6b) [77]. We also observe significant improvements in the sensitivity, detection limit, and range of linear response, relative to the Pt-NP electrode. The selectivity of the FePt alloy NPs for ascorbic acid is also found to be higher than pristine Pt NPs, in spite of the presence of other interference species including dopamine, uric acid, citric acid, glucose and NaCl [77].

Extending this simple synthetic approach, we produce other binary metallic systems as new materials for sensing application. For instance, FeM (M = Pt, Pd, Au) NPs have been synthesized by electrochemical deposition on Si substrate and their sensing performance for As(III) detection has been evaluated [78]. We also compare the properties of these alloy NPs with those of single-metal NPs (obtained with the same method), and observe notable enhancement for the alloy NPs. Fig. 7 compares the electrochemical

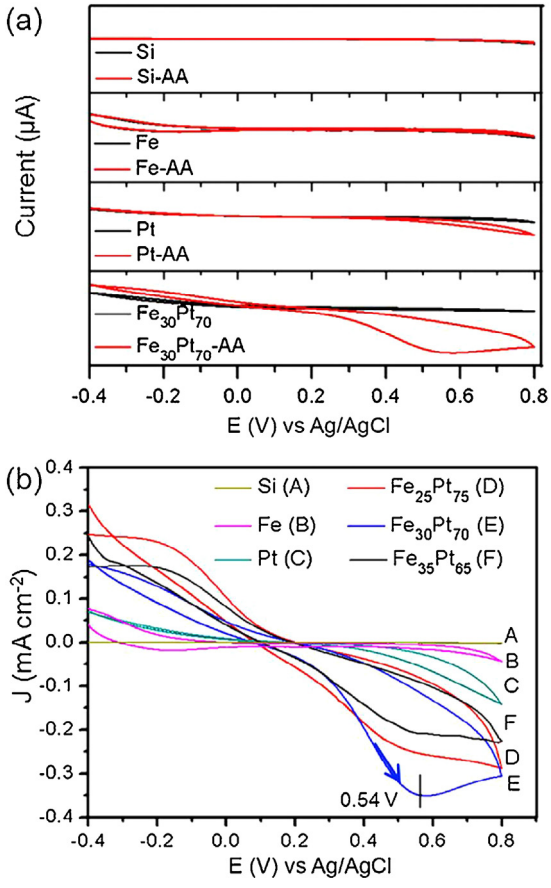

Fig. 6. (a) Cyclic voltammograms of a bare Si electrode, and electrodes electrodeposited with pristine Fe nanoparticles (NPs), pristine Pt NPs and $Fe_{30}Pt_{70}$ alloy NPs, all individually in a 10 mM phosphate buffer solution without and with 1 mM ascorbic acid (AA). (b) Cyclic voltammograms of Si electrode, electrodes with Fe NPs, Pt NPs, and $Fe_{25}Pt_{75}$, $Fe_{30}Pt_{70}$, and $Fe_{35}Pt_{65}$ alloy NPs in a 10 mM phosphate buffer solution with 1 mM AA. Scan rate is 50 mV s^{-1}.

Reprinted with permission from: N. Moghimi, K.T. Leung, Anal. Chem. 85 (2013) 5974–5980. Copyright (2013) by the American Chemical Society.

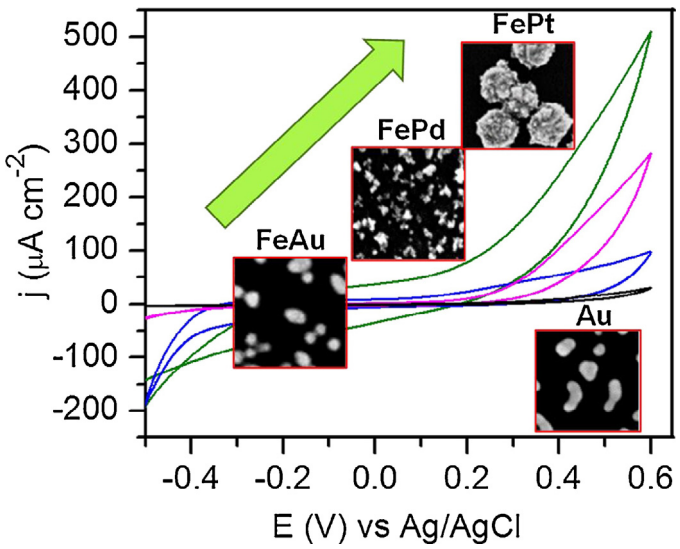

Fig. 7. Comparison of cyclic voltammograms of different bimetallic nanoparticles (NPs) for arsenic sensing. The voltammograms are obtained from different NPs deposited on Si substrates and used as electrodes in 10 mM PBS and 1 mM As solution. Scan rate is 50 mV s^{-1}. The FeAu NPs show better signal than the pristine Au NPs but worse than the FePd NPs, while the FePt NPs give the best response.

Reprinted with permission from: N. Moghimi, M. Mohapatra, K.T. Leung, Anal. Chem. 87 (2015) 5546–5552. Copyright (2015) by the American Chemical Society.

activity of different bimetallic NPs toward arsenic sensing based on their cyclic voltammetric response.

2.1.3. AuM (M = Pt, Ni)

AuPt alloy NPs are widely used as electro-catalysts, selective oxidants, and dehydrogenation catalysts [31,79]. The synthesis of single-phase AuPt alloy in the bulk is a big challenge because Au and Pt are immiscible [80]. However, theoretical studies for the heat of formation of AuPt alloy NPs have suggested that AuPt alloy could be prepared as nanoscale materials [81]. In this regime, AuPt alloy NPs are usually obtained by simultaneous reduction of the respective metal salt precursors by using reducing agents [82,83]. We produce AuPt alloy NPs and AuPt core-shell NPs (i.e., both Au on Pt and Pt on Au NPs) by electrochemical deposition [78,84], and demonstrate the superior sensor performance of AuPt alloy NPs compared to the AuPt core-shell NPs by using electro-oxidation of alcohol. We also show that the AuPt alloy NPs can be prepared by simply dip-casting our H-terminated Si substrate into an aqueous solution containing $AuCl_3$ and $PtCl_4$, which represents the simplest method ever reported for preparing the AuPt alloy NPs. Fig. 8 shows the schematic model for the formation of AuPt NPs and compares their sensing activity toward alcohol electro-oxidation with those of Pt/Au and Au/Pt core-shell NPs. Pt/Au NPs are obtained by electrodeposition of Au NPs in first step followed by electrodeposition of a Pt layer on the Au NPs in the second step, and vice versa for Au/Pt NPs.

In the case of Au and Ni, the large miscibility gap in the binary phase diagram of Au and Ni indicates that the AuNi alloy can only be formed at very high temperature [85]. In the nano-size regime, AuNi alloy NPs have also been prepared by simultaneous reduction of metal salt precursors with appropriate reduction [86,87] or by employing electrochemical deposition in a solution containing appropriate electrolytes to produce the AuNi alloy NPs [88]. However, the corresponding TEM analysis of a representative deposit in the reported work [88] only provided an electron diffraction pattern consistent with fcc Au that exhibited a preferred (111) orientation with a significant (200) reflection. The reported AuNi alloy

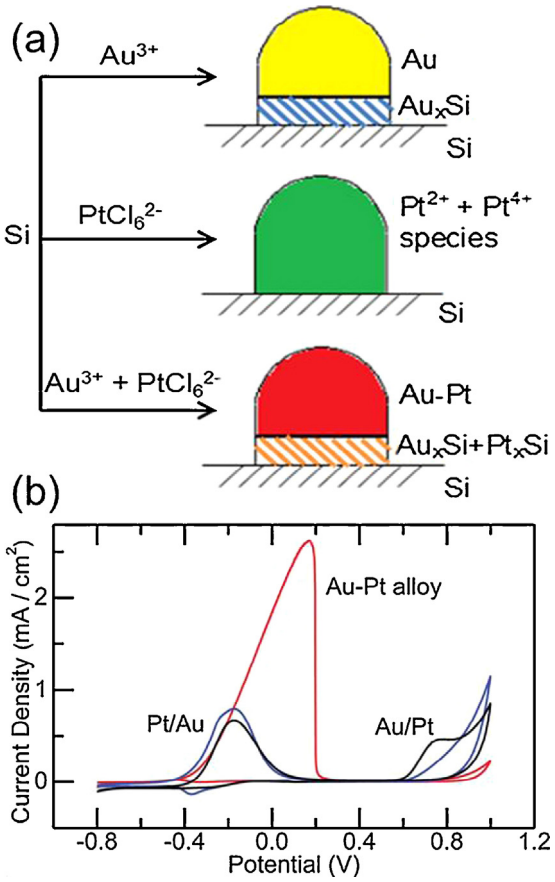

Fig. 8. (a) Schematic model for formation of AuPt NPs, (b) cyclic voltammogram of AuPt NPs compared to those of Au/Pt (Au shell on Pt core) and Pt/Au (Pt shell on Au core) core-shell NPs.

Reprinted with permission from: L.Y. Zhao, J.P. Thomas, N.F. Heinig, M. Abd-Ellah, X. Wang, K.T. Leung, J. Mater. Chem. C 2 (2014) 2707-2014. Copyright (2014) by the Royal Society of Chemistry.

exhibited a uniform gold texture (with a single-phase fcc structure) decorated with a few rectangular Ni nanoparticles, which suggests that the reported electrodeposits consisted of separated Au and Ni grains instead of the alloy as claimed. These studies highlighted some of the challenges in the nanoalloy literature, and extra care must therefore be taken in proper characterization of any declared alloy nanomaterials. We obtain AuNi alloy NPs by one-step electrodeposition onto a H-terminated Si(100) substrate, and compare these NPs with the nanodeposits obtained with two-step sequential electrochemical deposition [89]. These experiments provide evidence for a new catalytic growth mechanism, shown schematically in Fig. 9. In this autocatalytic mechanism, the initially formed Au nuclei act as the catalysts to promote the subsequent AuNi alloy growth. Confirmation of alloy formation has been provided by XPS analysis [89].

2.2. Metal–metal oxide

Nanoparticles have been supported on transition metal oxides in order to generate different properties from those of unsupported NPs. For example, Au NPs supported on metal oxides (e.g., TiO_2, Al_2O_3, Cr_2O_3, Fe_2O_3) have been found to exhibit enhanced catalytic activities [90,91]. For gas sensors, performance enhancement in sensitivity, stability and selectivity is achieved when noble metal NPs are deposited on the surfaces of metal oxides, such as tungsten oxide [92]. Au has become not only an extremely promising catalyst

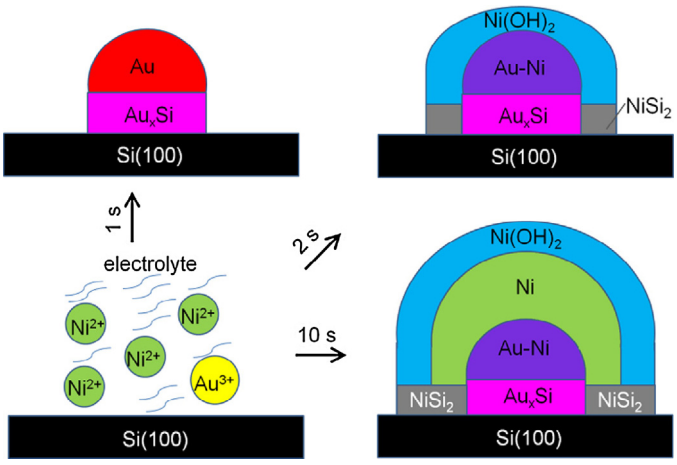

Fig. 9. Schematic model for autocatalytic growth mechanism of AuNi alloy NPs. Reprinted with permission from: L.Y. Zhao, N.F. Heinig, K.T. Leung, J. Phys. Chem. C 116 (2012) 12322–12329. Copyright (2012) by the American Chemical Society.

for a wide range of reactions (e.g., low-temperature CO oxidation), but also a high-efficiency sensor material that takes advantage of the surface plasmon and surface-enhanced Raman scattering effects, when the size decreases to the nanometer regime [93,94]. Au NPs have therefore been introduced onto different materials in order to enhance the sensing, photocatalytic, and optical properties of the host or support oxide materials. We have prepared Fe oxide and Zn oxide host nanostructures and coated them with Au NPs using the electrodeposition method. These hybrid materials are found to exhibit notable synergetic properties described below.

2.2.1. Fe oxide–Au

Fe and Fe oxides have been widely used as magnetic materials, catalysts, sensors, and drug delivery vehicles [95–98]. Hybridization of noble metal such as Au with Fe oxides provides synergetic effects in the aforementioned applications. For example, it has been extensively reported that Fe oxides and Au NPs could be combined to act as a catalyst for low-temperature CO oxidation ($CO + H_2O \rightarrow CO_2 + H_2$) [99–102]. For application as a biological sensor, poly(ethylenimine) functionalized graphene/Fe_3O_4 hybrids assembled with luminol-Au NPs have been used as a platform for the determination of HeLa cells [103]. Combining the magnetic property of Fe_3O_4 and the self-assembly property of pre-coated thiol Au NPs modified by nitrilotriacetic acid, the resulting Au—Fe_3O_4 NPs have been developed for protein separation [104]. Furthermore, the thickness of the Au shell has been manipulated in order to tune the plasmonic properties of the Fe oxide/Au core–shell nanostructures [105,106]. We synthesize Fe oxide NPs on a gold nanoisland template supported on Si and on a template of Au nanoislands prefunctionalized by 1,4-phenylene diisocyanide (PDI) [107]. Using electrochemical technique to investigate hybridization of Au and Fe oxide with and without PDI, we observe that PDI functionalization facilitates faster and easier hybridization, which enables the Au nanoislands to aggregate or relocate on top of the Fe oxide NPs upon applying a voltage. Fig. 10 shows the SEM images and schematic models of Fe electrodeposited on PDI-functionalized and on bare Au nanoisland templates, and of Au deposited on Fe nanorice particle template by magnetron sputtering and by electrodeposition. These models are compared with model for the preferential Fe deposition on larger Au islands. Hybridization of metal oxide (Fe oxide) on metal (Au) or of metal on metal oxide therefore depends on the size of the Au nanoislands relative to that of the Fe oxide NPs and on the presence or absence of a protective PDI shell around the Au nanoislands.

2.2.2. ZnO—Au

ZnO has been used as an alternative n-type semiconducting photoanode material for dye sensitized solar cells (DSSCs) because of their similar direct bandgap, higher electron dynamics, and versatile nanostructural morphologies when compared to TiO_2 [108–111]. Further modification has been performed by mixing with other nanostructured metal oxides such as TiO_2 and SnO_2 or with metallic NPs including gold and silver [112–115]. One of the major applications that utilize their improved light absorption capability specifically in the visible region is photovoltaics [116–119]. Surface modification with plasmonic NPs was first introduced in photovoltaics to enhance the performance of inorganic thin-film solar cells, particularly by compensating the loss of absorption with reduction in the absorber layer thickness [120–124]. In particular, Au NPs have been used in both polymer-based and dye-based organic photovoltaics to provide a significant enhancement in their performance [125–129]. We succeed in decorating the high-surface-area ZnO nanotubes obtained by direct electrodeposition with Au NPs using a successive electrodeposition procedure [130]. The resulting Au-NP decorated ZnO nanotube sample is then used as a DSSC photoanode. Electrodeposition is capable of preparing high-quality materials with better crystallinity and minimum lattice mismatch. The enhanced interface quality could also improve the contact of Au NPs on ZnO nanotube surface with lower resistance, therefore enabling better electron conduction that can be utilized for appropriate electronic device applications. Our results illustrate the advantages of electrodeposited Au-NP/ZnO-nanotube photoanode, provided by their better capacity for dye loading and higher charge transport efficiency inherent in the ZnO nanotubes and by pronounced enhancement in their absorption due to surface plasmons of the Au NPs. The overall enhancement can be clearly seen with the current–voltage characteristics and found to increase to 6.0% for Au-NP/ZnO-nanotube DSSC from 4.7% for pristine ZnO nanotube DSSC. Fig. 11 shows SEM images of ZnO nanotubes without and with different amounts of Au NP deposition, along with the schematic diagrams of the device architectures. The higher photon absorption and the increase in the short-circuit current density (one of the key performance indicators for DSSC) for the ZnO nanotubes decorated with Au NPs, when compared to pristine ZnO nanotubes, are clearly evident in Fig. 11. In another application, we have found that the Au-NPs/ZnO-nanotube hybrid system also exhibits better sensing properties for formic acid detection compared to pristine ZnO nanotubes. These results indicate that hybridization of ZnO nanotubes and metal NPs offers enhanced properties in sensing and solar cell applications.

2.3. Metal–biomolecule

Composite systems consisting of metal nanostructures and biomolecules combine the novel optical, electronic, and catalytic properties of nanomaterials with the evolution-optimized molecular recognition capability of biomolecules. These composite systems provide an excellent platform for building a new generation of multi-functional bioelectronic devices. In the past decade, substantial progress has been made in the use of biomolecule-nanostructure composite materials in electrochemical biosensors, electronic nanocircuitry and even nanodevices [12,131–133]. In the conventional approach, the biomolecules and metal nanostructures are treated as separate entities. Biomolecules are then immobilized on the inner and/or outer surfaces of the nanostructures, including polymer matrices, inorganic supports, and NPs [134–136]. Well-established techniques based on physical adsorption, electrostatic binding, specific recognition, and covalent coupling have often been used for immobilization [137–140]. For instance, adsorption of proteins on NPs has been achieved through

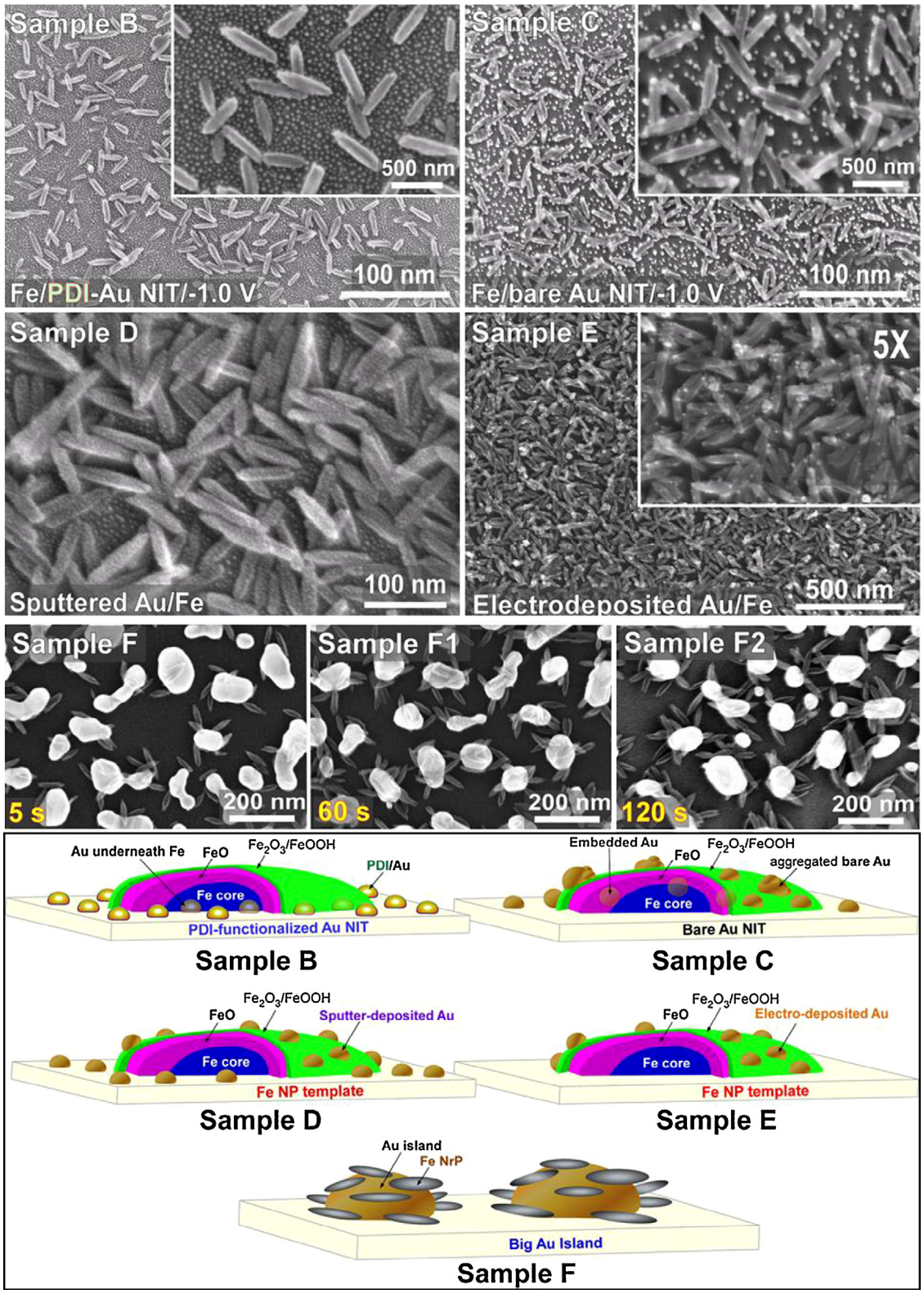

Fig. 10. Scanning electron microscopy images (upper panels) and schematic models (bottom panel) of Fe electrodeposited on PDI-functionalized (sample B) and bare Au nanoisland templates (sample C), and of Au deposited on Fe nanorice particle template by magnetron sputtering (sample D) and by electrodeposition (sample E), and of preferential Fe deposition on larger Au islands (sample F). The amounts of electrodeposition time are indicated for samples F, F1 and F2.

Reprinted with permission from: Y. Sohn, D. Pradhan, J.-S. Kang, K.T. Leung, RSC Adv. 5 (2015) 31472–31478. Copyright (2015) by the Royal Society of Chemistry.

electrostatic interactions between the partially charged amino acid side-groups of the protein and the appropriate components with opposite polarity on the NPs [141,142]. In contrast, relatively few studies on bio-integration into the nanostructure during growth have been made [18,143]. These studies can, however, provide fundamental information about the nature of this integration, including bonding, interactions, and growth mechanism, which could lead to a new class of bio-nanomaterials.

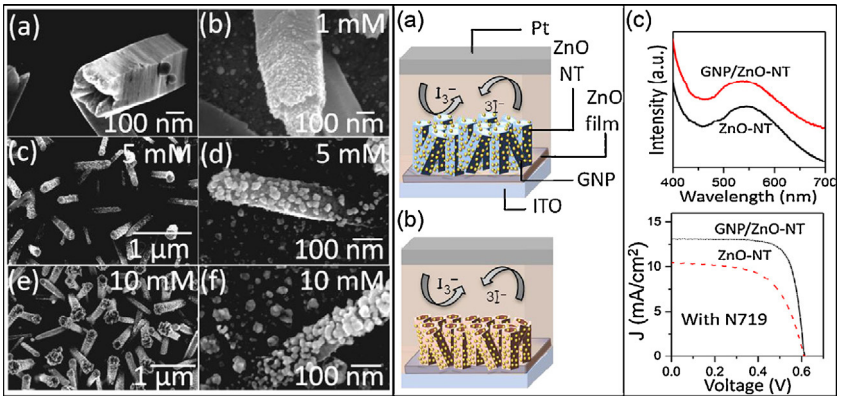

Fig. 11. Left panel: Scanning electron microscopy images of (a) pristine ZnO nanotubes, and Au-NPs/ZnO-nanotubes obtained by electrodeposition in (b) 1 mM, (c, d) 5 mM, and (e, f) 10 mM $AuCl_3$ electrolytes, all mixed with 0.1 M $NaClO_4$ and 0.1 M KCl supporting electrolyte, at room temperature. Right panel: Schematic diagrams of the solar cell device architectures, constructed from ZnO nanotubes (NTs) decorated with gold nanoparticles (GNPs) (a) without and (b) with N719 dye, illustrating the respective photon-to-electron conversion mechanisms, and (c) UV–Vis absorption spectra (upper graph) and short-circuit current density vs voltage curves (lower graph) for GNP/ZnO-NT and ZnO-NT solar cells.

Reprinted with permission from: M. Abd-Ellah, "Hybrid Transparent Conductive Oxide Nanostructured Materials for Photovoltaic Applications", Ph.D. Thesis, 2015, University of Waterloo.

Glucose oxidase (GOx, with MW of 160 kDa) is one of the most popular model biomolecules for studying the interactions between nanostructures and biomolecules. It also has many potential applications in biosensor research, food industry, and renewable fuel cells [144–148]. There are a limited number of studies on conjugating GOx onto NPs by electrostatic interaction [149,150], in which the NPs were synthesized first and GOx were subsequently immobilized on the NPs. Even in the earlier work on the co-electrodeposition of GOx and gold NPs [151,152], separate GOx and pre-grown NPs were used. Incorporation of biomolecules directly into the nanostructures during growth is extremely challenging, because an aqueous medium with a mild (neutral) pH and low growth temperature (below room temperature) is required to prevent the biomolecules from denaturing. However, these conditions are usually not conducive to nanostructure growth, which needs high temperature, and/or acidic or basic media for the crystal growth. Recently, we succeed in synthesizing Fe—GOx hybrid NPs by using Fe—GOx complexes directly as the building blocks, without the need to involve pre-grown Fe NPs [18]. These hybrid NPs consist of Fe nanocrystallites bound together by biomolecules in a stone-and-mortar architecture. We could obtain Fe–biomolecule complexes by adjusting the pH of the aqueous solution to above the isoelectric point of the biomolecule of interest. At this pH, amino acids on the surface of the biomolecule are negatively charged and interact electrostatically with the positively charged Fe ions.

We observe unique superparamagnetic properties for these hybrid NPs even when these hybrid NPs are as large as a few hundred nanometers. The Fe—GOx hybrid NPs also exhibit remarkable biocompatibility to human hepatoma cells (liver cells) while preserving the bioactivities of GOx at the same time. The same hybridization approach can also be easily extended to incorporate other biomolecules, even with dramatically different sizes, in these hybrid NPs. We use the anticancer p53 peptide (p53p, with MW of 1.8 kDa), which is a promising drug for most cancers because it can bind to both Mdm2 and MdmX in cancer cells [153]. The attachment of p53p to magnetic NPs that can be delivered to targeted tumor sites (drug-delivery vehicles) would be a breakthrough in anticancer therapeutics. We further demonstrate that p53p remains active after hybridization and it can bind to Mdm2. Isolation of Fe nanocrystallites by GOx or p53p introduces extraordinary magnetic property for large hybrid nanoparticles (i.e. superparamagnetism in large sizes) [18]. Fig. 12 shows the schematic model for NP formation involving Fe—GOx complexes as the building blocks. The middle panel illustrates the presence of all components of Fe and GOx along the depth direction of the NP, confirming the hybrid structure of the NP. The lower panel shows similar growth of HeLa cells on substrates with and without NPs, thus confirming the cell-friendly nature and bio-compatibility of these hybrid NPs.

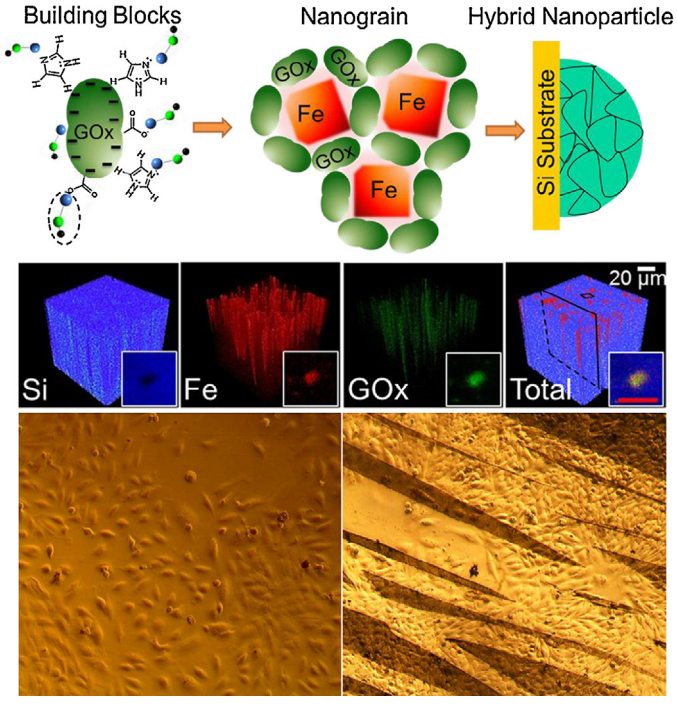

Fig. 12. Top panel: A schematic diagram of the "stone-and-mortar" model for Fe—GOx hybrid nanoparticles (NPs) electrodeposited on a Si substrate. Middle panel: TOF-SIMS 3D images of Si^+ (blue), Fe^+ (red), and $NaNH_2^+$ (corresponding to GOx; green), and their overlap (total) for Fe—GOx hybrid NPs on a $100 \times 100\ \mu m^2$ area of the sample, with the insets depicting their corresponding topmost 2D maps of a selected Fe—GOx hybrid NP in this sampling area (marked by a small square in the rightmost image). The scale bar for the insets is 2 μm. Lower panel: Optical images of HeLa cells grown on ITO-glass substrate coated with Fe—GOx hybrid NPs, 400 nm in average size, after 5 days without (left) and with sample scratching (right). The scratch marks (brighter areas on the right) correspond to the places without any NP. These images confirm similar amounts of cells grown on areas with and without NPs.

Reprinted with permission from: N. Moghimi, A.D. Donkor, M. Mohapatra, J.P. Thomas, Z. Su, X. Tang, K.T. Leung, J. Am. Chem. Soc. 136 (2014) 10478–10485. Copyright (2014) by the American Chemical Society.

2.4. Metal oxide–metal oxide

Mixed oxide nanostructures or metal oxide core-shells are often used to achieve or promote specific surface properties or to passivate an active material [154–160]. For instance, field emission enhancement has been observed in CuO nanowires coated with ZnO NPs [154]. Capacitive performance improvement was observed in TiO_2 nanotubes with molybdenum oxide coating [155], while SnO_2/TiO_2 double-shell nanotubes showed stable cycling and higher charge/discharge rate performance in lithium ion batteries [156]. The presence of a second oxide phase or the formation of mixed oxides can effectively change the bulk electronic arrangement and hence the charge carrier concentrations in the system [157]. The addition of foreign oxides induces new grain arrangements in the parent structure by creating new grain boundaries or by inducing porosity that leads to active sensing sites thereby increasing the overall response.

We have used the pulsed laser deposition method to produce SnO_2 oxide nanostructures with coating of a second oxide (e.g. NiO, TiO_2, ZnO). Pulsed laser deposition involves direct laser ablation of the target material into the gas phase, and the resulting gaseous material is then exposed to the substrate held at a preselected temperature. This deposition method accommodates the use of multiple targets without exposure to air and enables homo- and heteroepitaxial growth of nanostructures while preserving the stoichiometry of the target materials.

2.4.1. SnO_2—NiO

Recently, ZnO and SnO_2 are being used as alternative materials to TiO_2 in DSSC applications, due to their excellent optical transparencies, wide direct bandgaps, high electron mobility, and large electron diffusion coefficients [110,161]. However, ZnO could suffer from its lower chemical stability and dye loading capacity, making it less attractive as a photoanode material [162]. In contrast, SnO_2, with a bandgap of 3.8 eV, has lower UV degradation characteristic and generally better stability. The faster recombination rate of SnO_2 is, however, a major disadvantage, which can be alleviated by coating with a compact thin film of MgO as a passivation layer. We employ the pulsed laser deposition technique to produce novel SnO_2 hierarchical nanostructures by introducing NiO to create new nucleation sites [163]. This hybridization induces the growth of nanobelt side branches off the nanobelt main trunk to produce a highly branched structure with a much larger surface area. In addition, we achieve further tuning of the open-circuit voltage by simple surface passivation treatment of these hierarchical SnO_2 nanostructures with uniform coating of an MgO layer, with its thickness appropriately optimized. A 10-fold enhancement in the photon-to-electron conversion efficiency of the hierarchical SnO_2 nanostructured sample with MgO passivation (to 4.14%) relative to that of a pristine SnO_2 nanobelt sample has been achieved. Fig. 13 shows SEM images of pristine SnO_2 nanobelts, NiO—SnO_2 and MgO/NiO—SnO_2 hierarchical nanostructures, and the schematic diagram of the growth mechanism for NiO—SnO_2 hierarchical nanostructures. It also compares the performance of the cells with different photoanode materials.

2.4.2. SnO_2—TiO_2 and SnO_2—ZnO

Nanostructured material of ZnO, like TiO_2 and SnO_2, is a transparent semiconducting material that exhibits a high surface area to volume ratio, high biocompatibility, high stability, and low toxicity. Numerous biosensors employing ZnO have been reported for chemical analysis of a number of benchmark molecules related to key biochemical processes, including cholesterol, glucose, urea, cortisol, H_2O_2, and glutamate [164,165]. Using pulsed laser deposition, we deposit a very thin ZnO or TiO_2 layer on SnO_2 nanowires (pre-grown by pulsed laser deposition), instead of flat, planar surfaces, in order to increase the area of the electroactive surface. To compare their sensing properties with those of pristine SnO_2 nanowires, we perform cyclic voltammetry on all three samples. Cyclic voltammetry shows that all three electrodes, based on pristine, ZnO-coated, and TiO_2-coated SnO_2 nanowires, are sensitive to the addition of glucose to the electrolyte. ZnO-coated

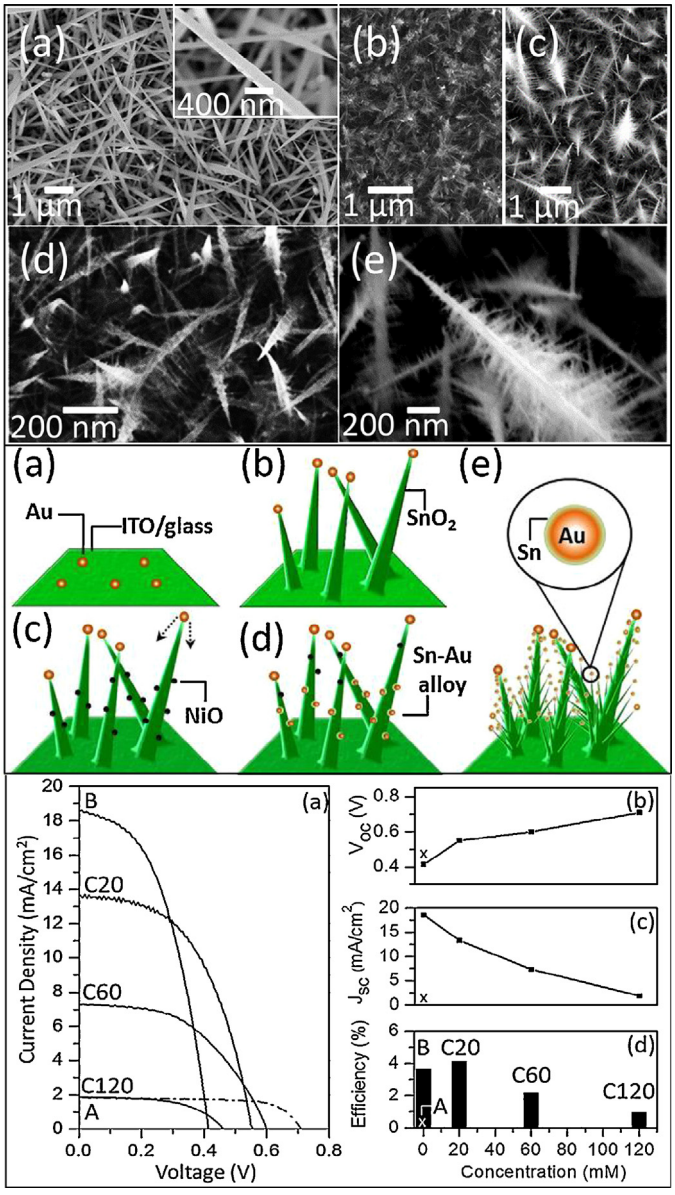

Fig. 13. Upper panel: Scanning electron microscopy images of (a) pristine SnO_2 nanobelts with inset at a higher magnification, (b, d) NiO—SnO_2 hierarchical nanostructures, and (c, e) MgO/NiO—SnO_2 hierarchical nanostructures (with the MgO passivation layer thickness appropriately optimized). All the nanostructures were grown by catalyst-assisted pulsed laser deposition on ITO-glass substrates predecorated with gold nanoislands at 500 °C in 400 mTorr of Ar for 90 min. Middle panel: (a–e) Schematic model of the growth mechanism for a typical NiO—SnO_2 hierarchical nanostructure grown by catalyst-assisted pulsed laser deposition using a SnO_2 target mixed with NiO. Lower panel: (a) Current density vs voltage profiles, (b) open-circuit voltage V_{OC}, (c) short-circuit current density J_{SC}, and (d) photon-to-electron conversion efficiency of DSSCs obtained with different photoanode materials: (cell A) pristine SnO_2 nanobelts (marked by cross), (cell B) NiO—SnO_2 hierarchical nanostructures, and (cell C20, C60, C120) NiO—SnO_2 hierarchical nanostructures passivated with MgO layers of different thicknesses.

Reprinted with permission from: M. Abd-Ellah, S. Bazargan, J.P. Thomas, Md A. Rahman, S. Srivastava, X. Wang, N.F. Heinig, K.T. Leung, Adv. Electronic Mater. 1 (2015) 1500032 (6 pp). Copyright (2015) by John Wiley and Sons, Inc.

SnO_2 nanowires exhibit the best result, with the limit of detection of almost 67 times better than that of pristine SnO_2 nanowires.

3. Type A + A′ materials: binary hybrid materials with two chemically identical components

Most of the synthesis methods are developed to produce one type of stoichiometrically identical material product, which is often polycrystalline and contains two or more phases. Indeed, controlling the growth conditions to obtain a perfect, single-crystalline material is one of the major challenges in materials science. For various applications, amorphous materials have shown better performance when compared to crystalline materials. Furthermore, enhancement in certain properties has been observed when imperfect materials are being used. We have divided these imperfect materials into three types: crystalline materials with two phases, consisting of either two different crystalline phases or a single crystalline phase and an amorphous phase; crystalline materials with a small amount of extrinsic impurities such as dopants; and crystalline materials with a small amount of intrinsic impurities such as defects that include cation vacancy and/or anion (e.g. oxygen) vacancy defects, or both.

3.1. Phase 1 + phase 2

Coexistence of two crystalline phases has led to different properties in the bimetallic or alloy systems [166]. In the case of nanocrystalline films of transparent oxides, the small size of the crystallites and their interconnections, as well as any gaseous species adsorbed on their large surface areas could significantly affect their electrical transport properties. In particular, the optical transmittance profiles of tin oxide films with different nanocrystallite sizes and crystalline-to-amorphous phase ratios are found to be quite different [167,168]. To illustrate different hybrid systems in this class (with the coexistence of two phases), we provide three examples of our work on binary-phase materials: SnO_2 nanocrystalline films, TiO_2 NPs, and FeNi bimetallic NPs, all of which exhibit different properties depending on their phase compositions. We use spin-casting for the preparation of SnO_2 film followed by post-annealing to obtain crystalline and amorphous SnO_2 at the same time. To produce well-ordered, precisely size-selected, monosized TiO_2 NPs with different crystalline-to-amorphous compositions, we employ a new fabrication process using a novel nanocluster magnetron sputter source with a built-in quadrupole mass filter. Finally, we use the electrodeposition method to obtain FeNi bimetallic NPs with different crystalline phases.

3.1.1. SnO_2

Gas sensors made from pristine or doped layers of SnO_2 have long been recognized to be not just cost-effective but also highly sensitive sensors. In addition to the porosity of the film that governs the amount of active surface area for the gas-sensing reaction, the gas-sensing properties of SnO_2 could be enhanced by decreasing the crystallite size below 10 nm for both pristine and doped SnO_2 films. Using a simple spin-casting followed by post-annealing procedure, we obtain a nanocrystalline SnO_2 film with different relative amounts of crystalline grains to amorphous regions [168]. Transmission electron microscopy and X-ray diffraction studies reveal that the onset of SnO_2 nanocrystallite formation in the amorphous film occurs at 350 °C. A narrow size distribution is obtained for the resulting nanocrystallites that are accompanied by the observed granular structures and voids throughout the film as a result of crystallization and grain growth. The average nanocrystallite size is found to slowly increase from 7 nm at 350 °C to 10 nm at 500 °C and to grow exponentially above a second onset at 500 °C. As shown in Fig. 14, conductivity measurement of these films shows that the film with a large volume of amorphous phase (i.e., the film post-annealed at 350 °C) is the most conductive [167]. The facile control of the average size of nanocrystallites in the desirable size regime (from 7 to 30 nm) in the presence of the amorphous phase by manipulating the post-oxygen-anneal temperature promises a low-cost, easily scalable fabrication method of SnO_2 film for gas-sensing and nanoelectronic applications [168].

3.1.2. TiO_2

Transition metal and metal oxide nanoclusters have attracted a lot of recent attention due to their numerous applications in catalysis, sensors, optoelectronic and magnetic devices [169–176]. The chemical properties of these nanoclusters can be tuned by controlling their cluster size and structure, with further optimization made possible by modifying the nature of nano-constituents often combinatorially. Since molecular beam technique has enabled the study of free, unsupported nanoclusters in the gas phase [177,178], various procedures have been developed to deposit transition metal nanoclusters onto substrates (or supports) by the gas-phase aggregation technique [179–182]. However, acquiring nearly monosized nanoclusters below 10 nm remains to be a very difficult task. We demonstrate, in Fig. 15, a new fabrication technique to produce well-ordered, precisely size-selected nanoclusters with excellent uniform coverage over a large area by using a novel nanocluster magnetron sputter source with a built-in quadrupole mass filter [183].

As one of the most studied transparent conductive oxides, with bandgaps of 3.0 eV for rutile and 3.2 eV for anatase structures [184], TiO_2 (and Ti itself) is of great importance to catalysis and nanoelectronics. The synthesis of stable, size-selected TiO_2 (and Ti) nanoclusters in a controlled way could offer new prospect for creating novel cluster-assembled materials with novel properties. We show that exceptional photocatalytic performance can be obtained from these high-quality monosized TiO_2 nanoclusters in a photoelectrochemical water-splitting reaction. Fig. 15 shows that among the different cluster sizes that we produce, the larger nanoclusters (8 nm) consist of a crystalline core surrounded by an amorphous shell, while the smaller nanoclusters (6 and 4 nm) below a critical size appear to be completely amorphous. The amorphous nature of the smaller nanoclusters gives rise to a higher density of defects, which work as trapping and recombination centers for the photogenerated electron–hole pairs. Evidently, the photocurrent density is found to be higher for the smaller nanoclusters, which could be attributed to the increase in the amount of defects and to the increase in the specific surface area. To confirm that amorphous TiO_2 nanoclusters are better suited for the water-splitting reaction, we prepare, in a separate experiment, a "post-annealed" TiO_2 nanoclusters sample by annealing the as-deposited 6-nm nanoclusters at 800 °C for 90 min in air. A substantial drop in the photocurrent density is observed for the post-annealed sample [183]. This is due to the reduction in the defect density as a result of improved crystallinity caused by annealing at a high temperature. The increase in the photocurrent density of the totally amorphous 6-nm nanoclusters with respect to that of the crystalline-core amorphous-shell 8-nm nanoclusters can therefore be attributed to this effect. On the other hand, the further enhancement found for the 4-nm nanoclusters with respect to the 6-nm nanoclusters, both of which are totally amorphous, is due to the effect arising from increase in the specific surface area.

3.1.3. FeNi

The phase diagram of FeNi alloy exhibits three distinct regions (bcc, fcc, and bcc + fcc). Coexistence of the bcc and fcc phases at room temperature is observed when the Ni content is between 5% and 72% [185], which greatly depends on the method of preparation [59,186–190]. Indeed, it is very difficult to make alloys with the

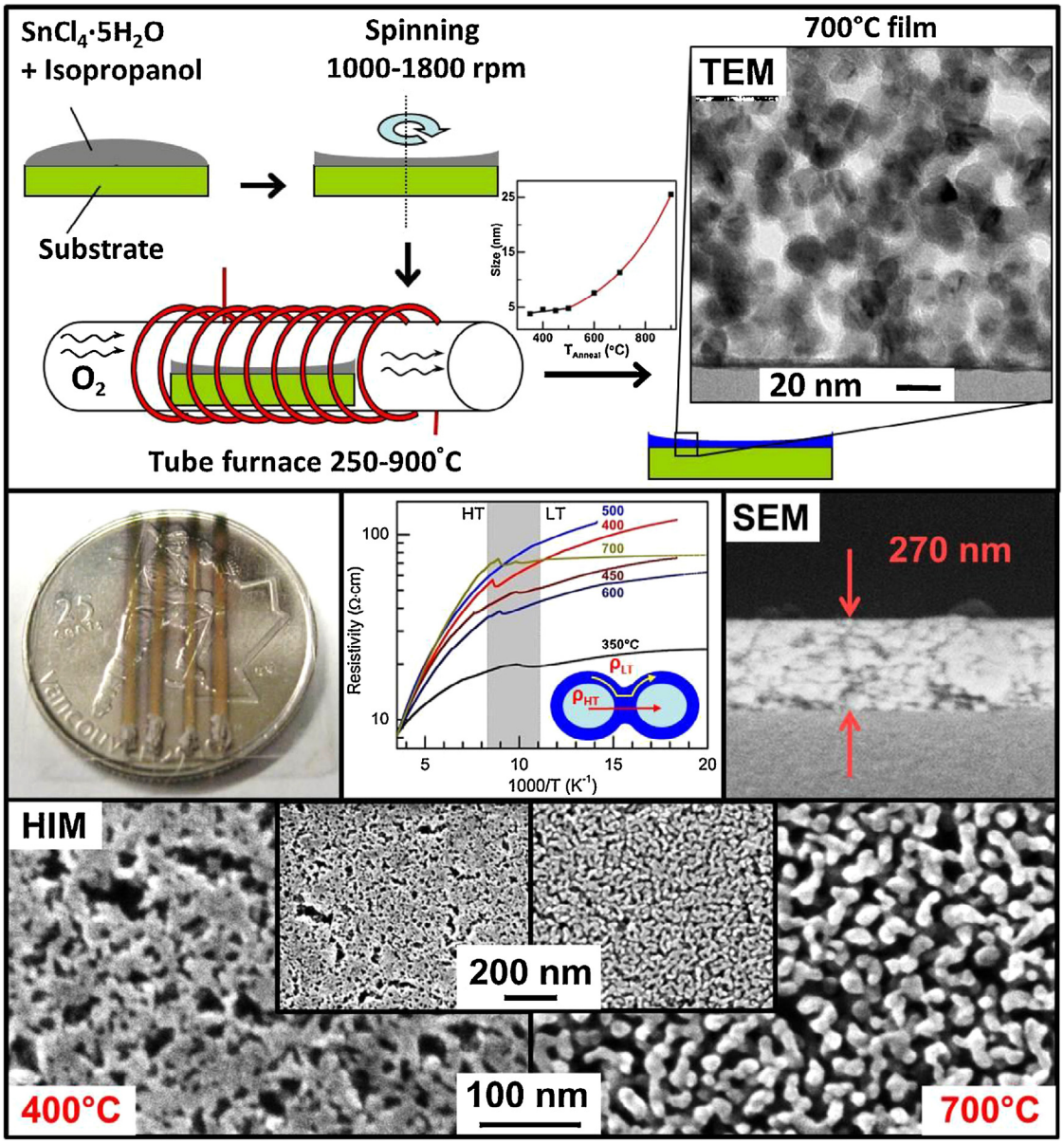

Fig. 14. Top: Schematic diagram of the preparation method of a nanocrystalline SnO_2 film, and TEM image of the film obtained with post-annealing at 700 °C. Middle-left: Photograph of a Canadian quarter under the SnO_2 film illustrating the transparency of the film and the four gold stripes deposited as contacts for the four-point probe resistivity measurement. Middle-center: Resistivity of the films obtained with post-annealing at different temperatures. Middle-right: SEM cross-sectional image depicting the thickness of the film. Bottom: Helium ion microscopy images depicting the morphology of the films obtained with post-annealing at 400 °C (left) and 700 °C (right).
Reprinted with permission from: S. Bazargan, N.F. Heinig, D. Pradhan, K.T. Leung, Cryst. Growth Des. 11 (2011) 247–255. Copyright (2011) by the American Chemical Society.

same composition by using different two-phase combinations in a single method. Recently, we succeed in synthesizing $Fe_{63}Ni_{37}$ alloy NPs with the same composition but two distinct shapes. In these two-phase alloy NPs, the combination of the two coexisting fcc and bcc phases is different for each shape [166]. This shape-dependent effect potentially provides a new control for the properties of an alloy with a specific elemental composition. We also provide the first investigation of the role of two-phase combinations in governing the magnetic properties in both bulk and nanoalloys using large-scale density function theory (DFT) calculations. Fig. 16 shows the SEM images of FeNi NPs with the same composition but two different shapes, which correspond to their different crystal structures obtained with different percentages of the fcc and bcc phases. The optimized ordered and disordered structures and the corresponding cohesive energies as well as the total magnetization are also shown.

3.2. Doping

Doping semiconductors with different elements is one of the most common strategies to improve various properties [191–196] such as photocatalytic performance, conductivity, thermal and thermoelectrical properties, and to introduce new properties such as magnetic properties (into nonmagnetic oxides or materials). Dopants are often used to increase the conductivity of semiconductors and to provide enhancement of their sensing properties. Many excellent review articles about the role of dopants in modifying semiconductor properties are available in the literature [191–196]. Most of the semiconductor photocatalysts have two major drawbacks: their relatively large energy bandgaps that hamper the exploitation of solar light in photocatalytic reactions, and their low quantum efficiencies for photocatalyzed reactions due to the high recombination rates of photogenerated electron–hole

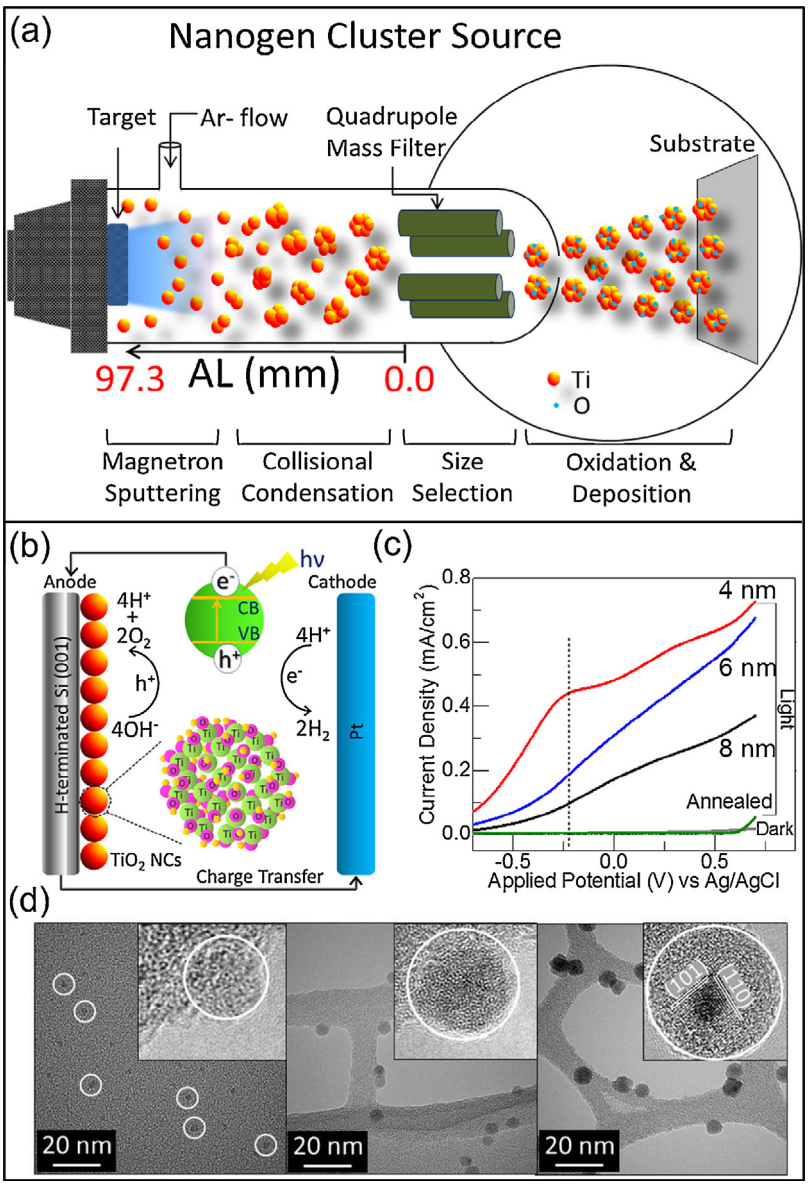

Fig. 15. (a) Schematic diagram of the creation and production of size-selected nanoclusters in the Nanogen cluster source and their deposition on the substrate. (b) Schematic diagram of the charge transfer mechanism involving the TiO_2 nanocluster (NC) photoanode. (c) Photocurrent densities as a function of applied potential obtained in a photoelectrochemical water splitting reaction in a 5 M KOH electrolyte, using TiO_2 nanoclusters of different sizes (4, 6 and 8 nm), all on H—Si, as the photoanodes, all with an illumination area of $5 \times 5\,mm^2$ under a 300 W Xe-lamp at a power density of 50 mW/cm^2. (d) TEM images of 4 nm (left), 6 nm (center) and 8 nm nanoclusters (right) deposited directly on holey carbon TEM grids.

Reprinted with permission from: S. Srivastava, J.P. Thomas, Md A. Rahman, M. Abd-Ellah, M. Mohapatra, D. Pradhan, N.F. Heinig, K.T. Leung, ACS Nano 8 (2014) 11891–11898. Copyright (2014) by the American Chemical Society.

pairs. We use spin-casting to dope Eu in SnO_2 films and the electrodeposition method to dope Eu into ZnO nanowalls, in order to change the photoluminescence properties of these oxides.

3.2.1. SnO_2—Eu

Point defects, e.g., anion deficiency and cation interstitial, in SnO_2 and other transparent conducting oxides could act as carrier generators, and their abundance could result in high levels of conductivity [197]. These defects have also been proposed to act as radiative recombination centers that contribute to the photoluminescence properties of these oxides in the visible region, in addition to their band-edge UV emission. In the past two decades, there has been growing interest in enhanced luminescence properties in nanostructured materials as a result of the quantum confinement effects [198] and/or of improved energy transfer from the host to the emission centers such as defect sites in these nanoscale structures [199,200]. In addition to creating defects in materials, incorporation of appropriate external dopants in these nanostructures is another promising approach to tuning the luminescence spectrum throughout the visible region, where dopant sites act as the recombination centers. Among the different possible dopants, rare earth transition metal ions, including those of Eu, Tb, Er, Ce, Tm, Ho, and Nd, are among the most attractive dopants, because their characteristic electronic transitions could lead to sharp luminescence features in the UV to infrared range [201,202]. The Eu^{3+} ion is of particular interest due to two characteristic orange emissions at ~614 nm and 593 nm, which correspond to an electric dipole transition ($^5D_0$–$^7F_2$) and a magnetic dipole transition ($^5D_0$–$^7F_1$), respectively.

In a systematic study of the effects of introducing Eu^{3+} dopants into nanocrystalline SnO_2 film on their physical and compositional

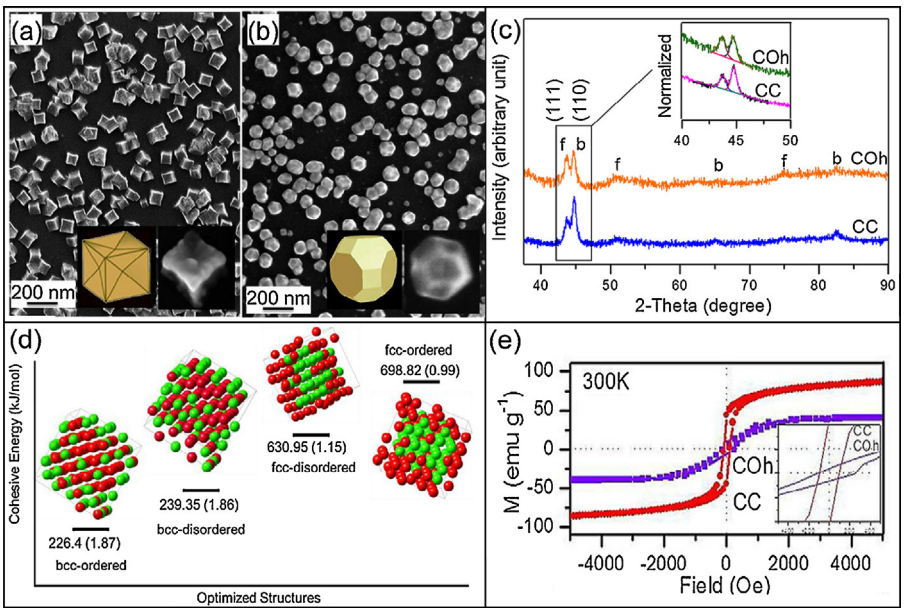

Fig. 16. (a, b) SEM images of $Fe_{63}Ni_{37}$ alloy NPs with two distinct concave cubic (CC) and cuboctahedron (COh) shapes, and (c) XRD patterns depicting the different amounts of bcc and fcc phases in the alloy NPs with the two different shapes. (d) Optimized calculated ordered and disordered structures and the corresponding cohesive energies (in unit of kJ/mol, not drawn to scale) and total moment (in parentheses, and in unit of μB/atom) for the most stable $Fe_{63}Ni_{37}$ supercells. (e) Hysteresis curves depicting different saturation magnetizations and coercivities for the alloy NPs with the two different shapes.

Reprinted with permission from: N. Moghimi, F.R. Rahsepar, S. Srivastava, N. Heinig, K.T. Leung, J. Mater. Chem. C 2 (2014) 6370–6375. Copyright (2014) by the Royal Society of Chemistry.

structures, we also investigate the dopant effect on the luminescence properties of these conductive nanocrystalline films [197]. Using a simple spin-casting technique, we incorporate Eu^{3+} ions homogeneously into the initially amorphous SnO_2 matrix beyond the solubility limit of crystalline SnO_2 (~0.06 mol.%) with concentrations as high as 20 mol.%. The latter is difficult to achieve using sol-gel and solvothermal methods [203]. Fig. 17 shows the TEM image and energy-dispersive X-ray maps of the Eu-doped SnO_2 film and the photoluminescence emission spectra of the pristine and Eu-doped SnO_2 samples obtained with excitation wavelength of 300 nm. Intense photoluminescence peaks characteristic of the Eu^{3+} emissions at 614 nm and 593 nm as well as defect-related emission peaks below 550 nm are observed for the homogeneously doped SnO_2 nanocrystallite film. The interplay between the SnO_2 nanocrystallites and the amorphous matrix/impurity phase leads to variation in the relative intensities of these peaks, which could be

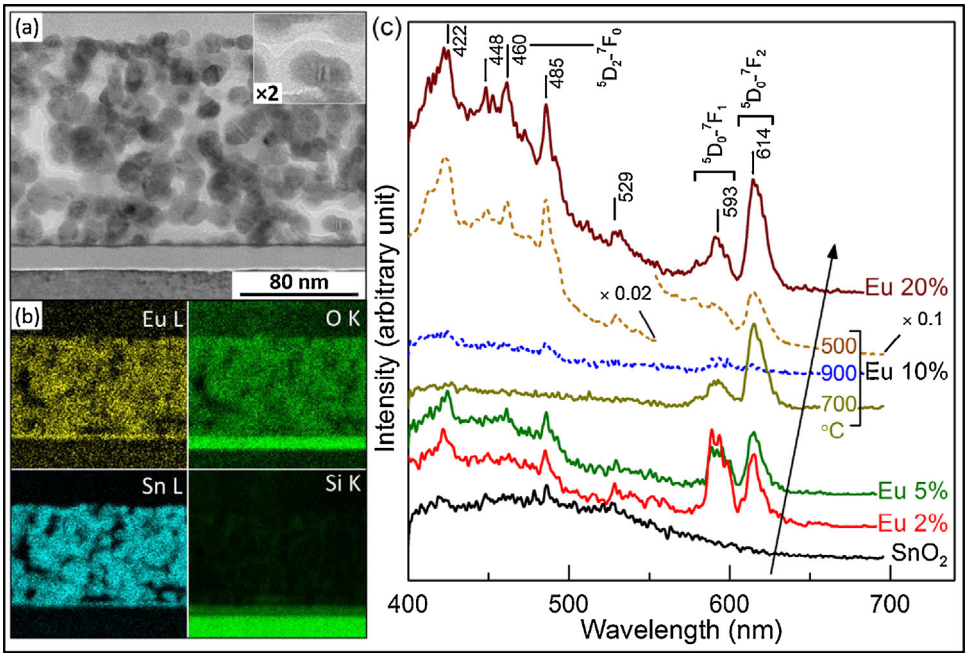

Fig. 17. (a) Scanning TEM image, and (b) energy-dispersive X-ray maps of Eu L, Sn L, O K, and Si K lines of a thin cross section of the Eu 2% doped SnO_2 film after post-annealed at 700 °C. Inset shows a magnified view of nanocrystallites surrounded by an amorphous layer. (c) Photoluminescence emission spectra of the pristine and Eu-doped SnO_2 samples obtained at excitation wavelength of 300 nm.

Reprinted with permission from: S. Bazargan, K.T. Leung, J. Chem. Phys. 137 (2012) 184704. Copyright (2012) by the American Institute of Physics.

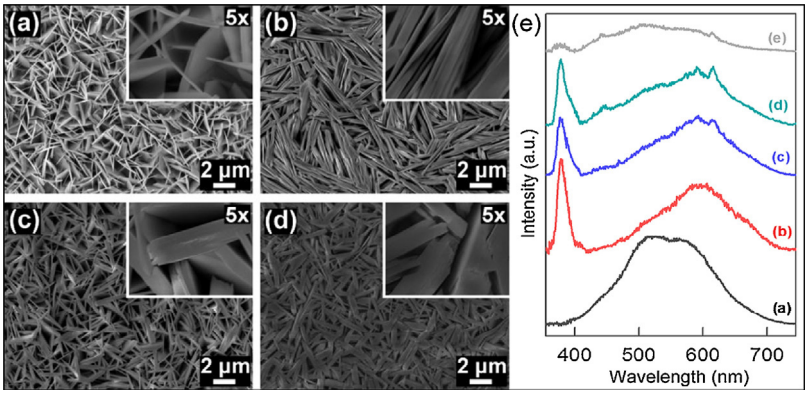

Fig. 18. SEM images of ZnO nanowalls deposited at 70 °C on ITO-glass in (a) 0.10 M $Zn(NO_3)_2{\cdot}6H_2O$ mixed with 0.10 M KCl, and with additional (b) 0.01 M, (c) 0.05 M, and (d) 0.10 M $Eu(NO_3)_3{\cdot}5H_2O$. (e) Photoluminescence emission spectra (with $\lambda_{excitation}$ = 325 nm) of (a) as-grown Eu^{3+}-doped ZnO nanowall sample surface-functionalized with 0.010 M 1,10-phenanthroline, and annealed samples surface-functionalized (b) without and with (c) 0.010 M, (d) 0.050 M, and (e) 0.10 M of phenanthroline.

Reprinted with permission from: J.-S. Kang, Y.-K. Jeong, J.-G. Kang, L. Zhao, Y. Sohn, D. Pradhan, K.T. Leung, J. Phys. Chem. C 119 (2015) 2142–2147. Copyright (2015) by the American Chemical Society.

manipulated by changing the dopant concentration and the post-anneal temperature. Our result shows that it is possible to obtain either a pure characteristic Eu^{3+} emission or a broadband emission containing both Eu^{3+} bands and defect-related bands for the same (10 mol.%) Eu-doped film by controlling the post-anneal temperature (700 °C for the former and 500 °C for the latter).

3.2.2. ZnO—Eu

Like SnO_2, rare-earth transition metal ion doped ZnO nanomaterials are recognized as promising candidates for applications in optoelectronic and light-emitting devices, and photocatalysis [204–207]. Upon excitation by UV irradiation, Eu-doped ZnO nanomaterials produce a band-edge emission at 369 nm, a broad defect-related emission at 500–750 nm and/or a red emission from Eu^{3+}. We fabricate ZnO nanowalls doped with various concentrations of Eu^{3+} on ITO-glass substrates by electrodeposition and investigate their photophysical properties [208]. We observe in Fig. 18 that the nanowalls become thicker and stacked upon doping with increasing amount of Eu. By functionalizing the surface of Eu^{3+}-doped ZnO nanowalls with an ultraviolet-range energy donor such as 1,10-phenanthroline, we investigate the energy transfer pathways in these nanowalls. This has allowed us to propose a cascade energy transfer model from ZnO to Eu^{3+} via phenanthroline, and obtain new insight into the emission and energy-transfer processes in surface-functionalized Eu^{3+}-doped ZnO nanostructures. Fig. 18 also shows the photoluminescence spectra of the Eu^{3+}-doped ZnO nanowalls before and after annealing, with and without surface-functionalization by phenanthroline. There are discernible changes in the blue-green emission at 600 nm upon Eu doping. These results show that the energy transfer from ZnO to Eu(III) appears to be extremely weak without phenanthroline, and provide strong support for our proposed cascade energy transfer model [208].

3.3. Crystal + defects

The structure and property changes in bulk or nanocrystalline materials caused by oxygen deficiency or anion vacancy defects have continued to attract a lot of attention. With appropriate control, it is possible to take advantage of these changes to produce materials with vastly different properties to benefit a variety of existing and emerging applications. For instance, ZnO NPs that contain a high concentration of oxygen vacancy defects exhibit an abnormally intense deep-level green emission over a wide wavelength range of 420–660 nm but negligible UV emission in its photoluminescence spectrum [209]. Recent studies also indicate that oxygen vacancy defects in TiO_x or TiO_xN_y (i.e., TiO_x with nitrogen doping) could improve charge transfer that significantly affects their electrochemical performance and oxygen reduction reactivity [210,211]. In addition, oxygen vacancy defects also play an important role in inducing ferromagnetism [212], changes in optical absorption properties [213], and phase separation [214]. Focusing on crystalline transparent oxides, we provide an example of structure and/or property modification by manipulation of oxygen vacancy defects. We illustrate the optical and electrochemical performance changes in TiO_x nanostructures obtained by pulsed laser deposition.

Pulsed laser deposition can be used to control not only the rate of deposition but also the crystallinity, morphology and amounts of anion (and cation) vacancy defects [215]. For metal oxides, oxygen vacancy defects play an important role because they could dramatically increase light absorption, and enhance the electrical conductivity and charge transport property by acting as electron donors [216,217]. The catalytic performance of metal oxide electrodes can therefore be improved significantly for photoelectrochemical water splitting reactions [183,218]. Using catalyst-assisted pulsed laser deposition under appropriate environment and growth temperature, we synthesize defect-rich one-dimensional TiO_2 nanostructures with a wide range of morphology (from nanoflakes to nanobelts to nanowires) on a Si substrate by controlling a SiO_2 buffer layer of appropriately optimized thickness and growth temperature [219]. Fig. 19 shows the different colors exhibited by these defect-rich samples: light blue for corrugated nanowires, dark blue for straight nanowires and grayish black for decorated nanowires, which can be attributed to the different amounts of defects and their respective degrees of sub-stoichiometry of TiO_2 in these nanostructured films [220]. Fig. 19 also compares the photoconversion efficiency measured as a function of the applied potential, in a photoelectrochemical water reaction under simulated sunlight (100 mW/cm^2), obtained from different TiO_2 nanostructured photoanodes. Evidently, the defect-rich decorated nanowires have the best photoelectrochemical catalytic performance, among all the TiO_2 nanostructured films. We also determine the photocurrent densities from separate UV and visible spectral illuminations. The photocurrent density for the decorated nanowires is found to mainly come from the visible light region (with wavelength greater than 430 nm), because we observe only a 13% reduction with just the visible light component. We demonstrate, for the first time, that these defect-rich one-dimensional nanostructures offer remarkable photocatalytic

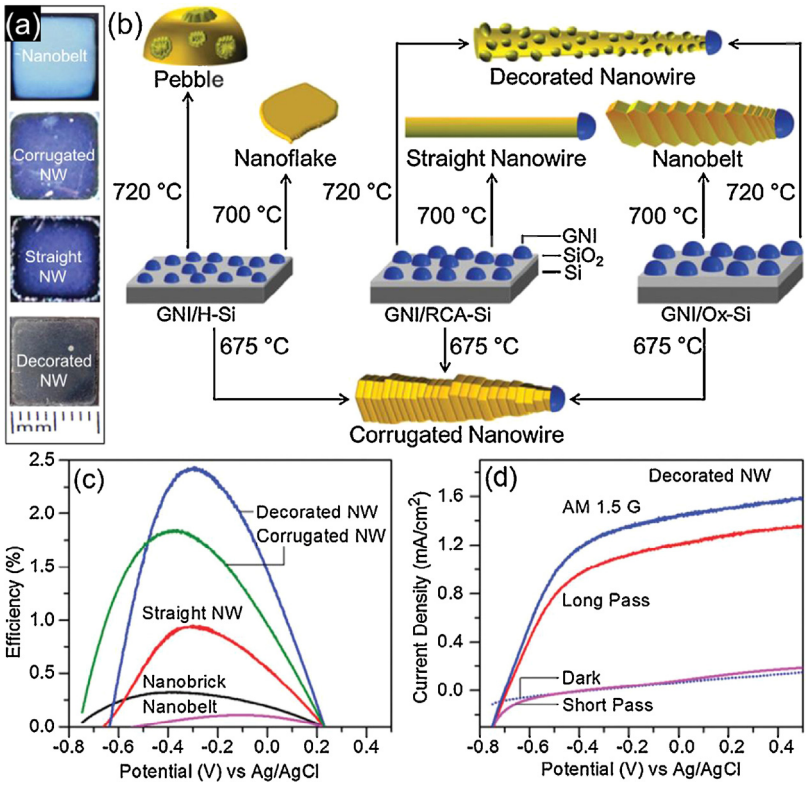

Fig. 19. (a) Photographs and (b) schematic models of TiO_2 nanostructured films consisting of nanobelts, corrugated nanowires (NWs), straight NWs, and decorated NWs grown on gold nanoisland (GNI) modified Si(100) templates at 675, 700 and 720 °C. (c) Corresponding photoconversion efficiency measured as a function of the applied potential from different TiO_2 nanostructured photoanodes. The measurements are performed in a 1 M KOH solution at a scan rate of 10 mV s^{-1} under 100 mW cm^{-2} simulated sunlight illumination by an AM 1.5G filter. (d) Linear sweep voltammograms of the decorated TiO_2 nanowire photoanode from an AM 1.5G light (100 mW cm^{-2}) and with long-pass (>430 nm) and short-pass (<400 nm) filters.

Reprinted with permission from: Md A. Rahman, S. Bazargan, S. Srivastava, X. Wang, M. Abd-Ellah, J.P. Thomas, N.F. Heinig, D. Pradhan, K.T. Leung, Energy Environ. Sci. 8 (2015) 3363–3373. Copyright (2015) by the Royal Society of Chemistry.

performance in the visible light region in a photoelectrochemical water-splitting reaction. This is a significant result because most of the transparent conductive oxides give decent photocurrent only in the UV range and the introduction of defects could therefore lead to significant performance improvement in these photocatalysts.

4. Concluding remarks

We have defined a new, perhaps broader, concept of hybridization for nanostructured materials by introducing a second component or characteristic or feature to the pristine material. These hybrid nanomaterials can be considered as consisting of two chemically different materials that are combined in different ways. They can also be considered as a single material that contains impure or imperfect physical constituent structures (which could be two crystalline phases), dopants or defects. Since imperfect materials (in terms of chemical purity, crystallinity, and stoichiometry) are widely available in nature, our focus here is to illustrate the many unique and novel properties that this hybridization could impart into the structure. Using examples from our recent work, we illustrate how various combinations of two constituent nanostructures could enhance different "target" properties when compared to the single-component nanostructures. These enhancements include better sensitivity and selectivity in sensors, higher efficiencies for solar cells and photoelectrochemical water splitting reactions, or better air stability (in alloy NPs). Novel magnetic properties are also observed when a metal such as Fe is hybridized with biomolecules or when different phases of FeNi are combined together. Introduction of dopants or defects also change the properties of the pristine nanostructures and make this kind of hybridization highly desirable for green energy applications. Hybridization is therefore a powerful general approach to new material fabrication and synthesis, particularly for the development of novel synergistic material properties.

Acknowledgement

This work was supported by the Natural Sciences and Engineering Research Council of Canada.

References

[1] A.K. Singh, Q. Xu, ChemCatChem 5 (2013) 652–676.
[2] M.P. Soriaga, Chem. Rev 90 (1990) 771–793.
[3] W.-L. Yim, T. Klüner, J. Phys. Chem. C 114 (2010) 7141–7152.
[4] V. Polshettiwar, R. Luque, A. Fihri, H. Zhu, M. Bouhrara, J.-M. Basset, Chem. Rev 111 (2011) 3036–3075.
[5] P.A. Derosa, J.M. Seminario, P.B. Balbuena, J. Phys. Chem. A 105 (2001) 7917–7925.
[6] G.-R. Li, Z.-S. Zhang, C.-Y. Su, Y.-X. Tong, J. Phys. Chem. C 113 (2009) 1227–1234.
[7] N.L. Rosi, D.A. Giljohann, C.S. Thaxton, A.K.R. Lytton-Jean, M.S. Han, C.A. Mirkin, Science 312 (2006) 1027–1030.
[8] P.M. Tessier, O.D. Velev, A.T. Kalambur, J.F. Rabolt, A.M. Lenhoff, E.W. Kaler, J. Am. Chem. Soc 122 (2000) 9554–9555.
[9] R. Ferrando, J. Jellinek, R.L. Johnston, Chem. Rev 108 (2008) 845–910.
[10] M.B. Cortie, A.M. McDonagh, Chem. Rev 111 (2011) 3713–3735.
[11] R. Costi, A.E. Saunders, U. Banin, Angew. Chem. Int. Ed. Engl 49 (2010) 4878–4897.
[12] E. Katz, I. Willner, Angew. Chem. Int. Ed. Engl 43 (2004) 6042–6108.
[13] P.D. Cozzoli, T. Pellegrino, L. Manna, Chem. Soc. Rev 35 (2006) 1195–1208.
[14] H. Zeng, S. Sun, Adv. Funct. Mater 18 (2008) 391–400.
[15] J. Gu, Y.-W. Zhang, F. (Feng) Tao, Chem. Soc. Rev 41 (2012) 8050–8065.
[16] X. Liu, D. Wang, Y. Li, Nano Today 7 (2012) 448–466.

[17] M. Sankar, N. Dimitratos, P.J. Miedziak, P.P. Wells, C.J. Kiely, G.J. Hutchings, Chem. Soc. Rev 41 (2012) 8099–8139.
[18] N. Moghimi, A.D. Donkor, M. Mohapatra, J.P. Thomas, Z. Su, X. Tang, et al., J. Am. Chem. Soc 136 (2014) 10478–10485.
[19] T. Krenke, E. Duman, M. Acet, E.F. Wassermann, X. Moya, L. Mañosa, et al., Nat. Mater 4 (2005) 450–454.
[20] H.-L. Jiang, Q. Xu, J. Mater. Chem 21 (2011) 13705.
[21] D. Ferrer, A. Torres-Castro, X. Gao, S. Sepulveda-Guzman, U. Ortiz-Mendez, M. Jose-Yacaman, Nano Lett 7 (2007) 1701–1705.
[22] M.C. Fromen, J. Morillo, M.J. Casanove, P. Lecante, Europhys. Lett 73 (2006) 885–891.
[23] F. Baletto, C. Mottet, R. Ferrando, Phys. Rev. Lett 90 (2003) 135504.
[24] B. Schrick, J.L. Blough, A.D. Jones, T.E. Mallouk, Chem. Mater 14 (2002) 5140–5147.
[25] D.A. Hansgen, D.G. Vlachos, J.G. Chen, Nat. Chem 2 (2010) 484–489.
[26] X. Ji, K.T. Lee, R. Holden, L. Zhang, J. Zhang, G.A. Botton, et al., Nat. Chem 2 (2010) 286–293.
[27] H. Kobayashi, M. Yamauchi, H. Kitagawa, Y. Kubota, J. Am. Chem. Soc 132 (2010) 5576–5577.
[28] F. Studt, F. Abild-Pedersen, T. Bligaard, R.Z. Sørensen, C.H. Christensen, J.K. Nørskov, Science 320 (2008) 1320–1322.
[29] Y. Tee, E. Grulke, D. Bhattacharyya, Ind. Eng. Chem. Res 44 (2005) 7062–7070.
[30] X. Teng, H. Yang, Front. Chem. Eng. China 4 (2010) 45–51.
[31] C. Burda, X. Chen, R. Narayanan, M.A. El-Sayed, Chem. Rev 105 (2005) 1025–1102.
[32] J. Liu, A.I. Maaroof, L. Wieczorek, M.B. Cortie, Adv. Mater 17 (2005) 1276–1281.
[33] J. Park, J. Joo, S.G. Kwon, Y. Jang, T. Hyeon, Angew. Chem. Int. Ed. Engl 46 (2007) 4630–4660.
[34] T. Mokari, A. Aharoni, I. Popov, U. Banin, Angew. Chem. Int. Ed. Engl 45 (2006) 8001–8005.
[35] X. Lu, L. Au, J. McLellan, Z.-Y. Li, M. Marquez, Y. Xia, Nano Lett 7 (2007) 1764–1769.
[36] J.C. Hulteen, J. Vac. Sci. Technol. A 13 (1995) 1553.
[37] Y. Wang, R.M. Hernandez, D.J. Bartlett, J.M. Bingham, T.R. Kline, A. Sen, et al., Langmuir 22 (2006) 10451–10456.
[38] S.R. Nicewarner-Pena, R.G. Freeman, B.D. Reiss, L. He, D.J. Pena, I.D. Walton, et al., Science 294 (2001) 137–141.
[39] Y. Mizukoshi, T. Fujimoto, Y. Nagata, R. Oshima, Y. Maeda, J. Phys. Chem. B 104 (2000) 6028–6032.
[40] C. Kan, W. Cai, C. Li, L. Zhang, H. Hofmeister, J. Phys. D Appl. Phys 1609 (2003) 1609–1614.
[41] J. Belloni, M. Mostafavi, H. Remita, J.-L. Marignier, M.-O. Delcourt, New J. Chem 22 (1998) 1239–1255.
[42] M. Gaudry, M. Pellarin, J. Vialle, M. Broyer, Phys. Rev. B 62 (2000) 5179–5185.
[43] G. Mattei, C. Maurizio, P. Mazzoldi, F. D'Acapito, G. Battaglin, E. Cattaruzza, et al., Phys. Rev. B 71 (2005) 195418.
[44] F. Baletto, R. Ferrando, D. Fisica, U. Genova, Rev. Mod. Phy 77 (2005) 317–423.
[45] W. de Heer, Rev. Mod. Phys 65 (1993) 611–676.
[46] C. Binns, Surf. Sci. Rep 44 (2001) 1–49.
[47] M.T. Reetz, W. Helbig, S.A. Quaiser, Chem. Mater 7 (1995) 2227–2228.
[48] U. Kolb, S.A. Quaiser, M. Winter, M.T. Reetz, Chem. Mater 8 (1996) 1889–1894.
[49] C.-B. Wang, W. Zhang, Environ. Sci. Technol 31 (1997) 2154–2156.
[50] I. Ban, M. Drofenik, D. Makovec, J. Magn. Magn. Mater 307 (2006) 250–256.
[51] H. Wang, J. Li, X. Kou, L. Zhang, J. Cryst. Growth 310 (2008) 3072–3076.
[52] Y. Chen, H. She, X. Luo, G.-H. Yue, W.-B. Mi, H.-L. Bai, et al., J. Nanosci. Nanotechnol 10 (2010) 3053–3059.
[53] B. Lu, H. Huang, X.L. Dong, X.F. Zhang, J.P. Lei, J.P. Sun, et al., J. Appl. Phys 104 (2008) 114313.
[54] X.L. Dong, Z.D. Zhang, X.G. Zhao, Y.C. Chuang, J. Mater. Res 109 (1999) 7203–7207.
[55] S. Vitta, A. Khuntia, G. Ravikumar, D. Bahadur, J. Magn. Magn. Mater 320 (2008) 182–189.
[56] B. Rao, S. Ramos de Debiaggi, P. Jena, Phys. Rev. B 64 (2001) 1–6.
[57] W. Shen, F.E. Huggins, N. Shah, G. Jacobs, Y. Wang, X. Shi, et al., Appl. Catal. A 351 (2008) 102–110.
[58] S. Behrens, H. Bönnemann, N. Matoussevitch, A. Gorschinski, E. Dinjus, W. Habicht, et al., J. Phys. Condens. Matter 18 (2006) S2543–S2561.
[59] N. Moghimi, S. Bazargan, D. Pradhan, K.T. Leung, J. Phys. Chem. C 117 (2013) 4852–4858.
[60] C.M. Wang, D.R. Baer, J.E. Amonette, M.H. Engelhard, Y. Qiang, J. Antony, Nanotechnology 18 (2007) 255603.
[61] A. Shavel, B. Rodríguez-González, M. Spasova, M. Farle, L.M. Liz-Marzán, Adv. Funct. Mater 17 (2007) 3870–3876.
[62] S.M. Ponder, J.G. Darab, J. Bucher, D. Caulder, I. Craig, L. Davis, et al., Chem. Mater 13 (2001) 479–486.
[63] M.H. Xu, W. Zhong, X.S. Qi, C.T. Au, Y. Deng, Y.W. Du, J. Alloys Compd 495 (2010) 200–204.
[64] M. Ammar, F. Mazaleyrat, J.P. Bonnet, P. Audebert, A. Brosseau, G. Wang, et al., Nanotechnology 18 (2007) 285606 (8pp).
[65] N. Moghimi, M. Abd-Ellah, J.P. Thomas, M. Mohapatra, K.T. Leung, J. Am. Chem. Soc 135 (2013) 10958–10961.
[66] W.H. Yang, D.J. Srolovitz, J. Mech. Phys. Solids 42 (1994) 1551–1574.
[67] D. Hernandez-Santos, M.B. Gonzalez-Garcia, A.C. Garcìa, Electroanalysis 14 (2002) 1225–1235.
[68] J.H. He, Q. Xu, Z.R. Song, H.Y. Kuang, Appl. Mech. Mater 110–116 (2012) 1732–1735.
[69] J.C. Claussen, A. Kumar, D.B. Jaroch, M.H. Khawaja, A.B. Hibbard, D.M. Porterfield, et al., Adv. Funct. Mater 22 (2012) 3399–3405.
[70] X. Bo, J.C. Ndamanisha, J. Bai, L. Guo, Talanta 82 (2010) 85–91.
[71] C. Su, C. Zhang, G. Lu, C. Ma, Electroanalysis 22 (2010) 1901–1905.
[72] N. Zhu, Z. Chang, P. He, Y. Fang, Anal. Chim. Acta 545 (2005) 21–26.
[73] R.S. Dey, C.R. Raj, J. Phys. Chem. C 114 (2010) 21427–21433.
[74] J.A. Gilbert, N.N. Kariuki, R. Subbaraman, A.J. Kropf, M.C. Smith, E.F. Holby, et al., J. Am. Chem. Soc 134 (2012) 14823–14833.
[75] C. Wang, H. Daimon, S. Sun, Nano Lett 9 (2009) 1493–1496.
[76] J. Kim, Y. Lee, S. Sun, J. Am. Chem. Soc 132 (2010) 4996–4997.
[77] N. Moghimi, K.T. Leung, Anal. Chem 85 (2013) 5974–5980.
[78] N. Moghimi, M. Mohapatra, K.T. Leung, Anal. Chem 87 (2015) 5546–5552.
[79] A. Villa, D. Wang, D.S. Su, L. Prati, Catal. Sci. Technol 5 (2015) 55–68.
[80] M. Mirdamadi-esfahani, M. Mostafavi, B. Keita, L. Nadjo, P. Kooyman, H. Remita, Gold Bull 43 (2010) 49–56.
[81] S. Xiao, W. Hu, W. Luo, Y. Wu, X. Li, H. Deng, Eur. Phys. J. B 54 (2006) 479–484.
[82] E.R. Essinger-Hileman, D. DeCicco, J.F. Bondi, R.E. Schaak, J. Mater. Chem 21 (2011) 11599–11604.
[83] A. Habrioux, W. Vogel, M. Guinel, L. Guetaz, K. Servat, B. Kokoh, et al., Phys. Chem. Chem. Phys 11 (2009) 3573–3579.
[84] L. Zhao, J.P. Thomas, N.F. Heinig, M. Abd-Ellah, X. Wang, K.T. Leung, J. Mater. Chem. C 2 (2014) 2707–2714.
[85] T.B. Massalski, Binary Alloy Phase Diagrams, ASM International, Ohio, USA, 1990.
[86] Y. Vasquez, Z. Luo, R.E. Schaak, J. Am. Chem. Soc 130 (2008) 11866–11867.
[87] S. Zhou, H. Yin, V. Schwartz, Z. Wu, D. Mullins, B. Eichhorn, et al., Chemphyschem 9 (2008) 2475–2479.
[88] A. Dolati, M. Ghorbani, M.R. Ahmadi, J. Electroanal. Chem 577 (2005) 1–8.
[89] L. Zhao, N. Heinig, K.T. Leung, J. Phys. Chem. C 116 (2012) 12322–12329.
[90] D. Widmann, R.J. Behm, Acc. Chem. Res 47 (2014) 740–749.
[91] H.-J. Freund, G. Pacchioni, Chem. Soc. Rev 37 (2008) 2224–2242.
[92] S. Vallejos, P. Umek, T. Stoycheva, F. Annanouch, E. Llobet, X. Correig, et al., Adv. Funct. Mater 23 (2013) 1313–1322.
[93] A.S.K. Hashmi, G.J. Hutchings, Angew. Chemie. Int. Ed 45 (2006) 7896–7936.
[94] S. Eustis, M.A. El-Sayed, Chem. Soc. Rev 35 (2006) 209–217.
[95] L. Machala, R. Zboril, A. Gedanken, J. Phys. Chem. B 111 (2007) 4003–4018.
[96] A. Gonzalez-De-Castro, C.M. Robertson, J. Xiao, J. Am. Chem. Soc 136 (2014) 8350–8360.
[97] J. Gallo, N. Kamaly, I. Lavdas, E. Stevens, Q.-D. Nguyen, M. Wylezinska-Arridge, et al., Angew. Chem. Int. Ed. Engl 53 (2014) 1–6.
[98] S. Laurent, D. Forge, M. Port, A. Roch, C. Robic, L. Vander Elst, et al., Chem. Rev 108 (2008) 2064–2110.
[99] N.M. Gupta, A.K. Tripathi, Gold Bull 34 (2001) 120–128.
[100] R. Finch, N. Hodge, G. Hutchings, A. Meagher, Q. Pankhurst, M. Siddiqui, et al., Phys. Chem. Chem. Phys 1 (1999) 485–489.
[101] M. Khoudiakov, M.C. Gupta, S. Deevi, Nanotechnology 15 (2004) 987–990.
[102] N.A. Hodge, C.J. Kiely, R. Whyman, M.R.H. Siddiqui, G.J. Hutchings, Q.A. Pankhurst, et al., Catal. Today 72 (2002) 133–144.
[103] W. Gu, X. Deng, X. Gu, X. Jia, B. Lou, X. Zhang, et al., Anal. Chem 87 (2015) 1876–1881.
[104] J. Bao, W. Chen, T. Liu, Y. Zhu, P. Jin, L. Wang, et al., ACS Nano 1 (2007) 293–298.
[105] H. Wang, D.W. Brandl, F. Le, P. Nordlander, N.J. Halas, Nano Lett 6 (2006) 827–832.
[106] Z. Xu, Y. Hou, S. Sun, J. Am. Chem. Soc 129 (2007) 8698–8699.
[107] Y. Sohn, D. Pradhan, J.-S. Kang, K.T. Leung, RSC Adv 5 (2015) 31472–31478.
[108] J.A. Anta, E. Guillén, R. Tena-Zaera, J. Phys. Chem. C 116 (2012) 11413–11425.
[109] M. McCune, W. Zhang, Y. Deng, Nano Lett 12 (2012) 3656–3662.
[110] S.H. Ko, D. Lee, H.W. Kang, K.H. Nam, J.Y. Yeo, S.J. Hong, et al., Nano Lett 11 (2011) 666–671.
[111] M. Abd-Ellah, N. Moghimi, L. Zhang, N.F. Heinig, L. Zhao, J.P. Thomas, et al., J. Phys. Chem. C 117 (2013) 6794–6799.
[112] C.-H. Ku, C.-H. Ku, J.-J. Wu, J.-J. Wu, Appl. Phys. Lett 91 (2007) 093117.
[113] R. Bhattacharjee, I.-M. Hung, ECS Solid State Lett 2 (2013) Q101–Q104.
[114] C.K.N. Peh, L. Ke, G.W. Ho, Mater. Lett 64 (2010) 1372–1375.
[115] S.D. Standridge, G.C. Schatz, J.T. Hupp, Langmuir 25 (2009) 2596–2600.
[116] D. Li, J.T. McCann, M. Gratt, Y. Xia, Chem. Phys. Lett 394 (2004) 387–391.
[117] C.S. Chou, R.Y. Yang, C.K. Yeh, Y.J. Lin, Powder Technol 194 (2009) 95–105.
[118] H.A. Atwater, A. Polman, Nat. Mater 9 (2010) 205–213.
[119] R.A. Pala, J. White, E. Barnard, J. Liu, M.L. Brongersma, Adv. Mater 21 (2009) 3504–3509.
[120] Y.A. Akimov, K. Ostrikov, E.P. Li, Plasmonics 4 (2009) 107–113.
[121] P. Spinelli, V.E. Ferry, J. van de Groep, M. van Lare, M.A. Verschuuren, R.E.I. Schropp, et al., J. Opt 14 (2012) 024002.
[122] V.E. Ferry, M.A. Verschuuren, H.B.T. Li, E. Verhagen, R.J. Walters, R.E.I. Schropp, et al., Opt. Express 18 (2010) A237–A245.
[123] V.E. Ferry, J.N. Munday, H.A. Atwater, Adv. Mater 22 (2010) 4794–4808.
[124] S. Pillai, M.A. Green, Sol. Energy Mater. Sol. Cells 94 (2010) 1481–1486.
[125] E. Stratakis, E. Kymakis, Mater. Today 16 (2013) 133–146.
[126] J. Zhu, M. Xue, H. Shen, Z. Wu, S. Kim, J.J. Ho, et al., Appl. Phys. Lett 98 (2011) 151110.
[127] F.C. Chen, J.L. Wu, C.L. Lee, Y. Hong, C.H. Kuo, M.H. Huang, Appl. Phys. Lett 95 (2009) 013305.
[128] V. Kochergin, L. Neely, C.Y. Jao, H.D. Robinson, Appl. Phys. Lett 98 (2011) 133305.
[129] Q. Gan, F.J. Bartoli, Z.H. Kafafi, Adv. Mater 25 (2013) 2385–2396.

[130] M. Abd-Ellah, Hybrid Transparent Conductive Oxide Nanostructured Materials for Photovoltaic Applications, Ph.D. Thesis; University of Waterloo, 2015.
[131] C.M. Niemeyer, Angew. Chem. Int. Ed. Engl 40 (2001) 4128–4158.
[132] E. Katz, L. Sheeney-Haj-Ichia, I. Willner, Chemistry (Easton) 8 (2002) 4138–4148.
[133] S. Mornet, A. Vekris, J. Bonnet, E. Duguet, F. Grasset, J.H. Choy, et al., Materials Lett 42 (2000) 183–188.
[134] T.K. Indira, P.K. Lakshmi, Int. J. Pharm. Sci. Nanotechnol 3 (2010) 1035–1042.
[135] C.-C. Yu, Y.-Y. Kuo, C.-F. Liang, W.-T. Chien, H.-T. Wu, T.-C. Chang, et al., Bioconjug. Chem 23 (2012) 714–724.
[136] S.A. Ansari, Q. Husain, Biotechnol. Adv 30 (2012) 512–523.
[137] T.E. Saraswati, A. Ogino, M. Nagatsu, Carbon N. Y. 50 (2012) 1253–1261.
[138] Z.-C. Xing, Y. Chang, I.-K. Kang, Sci. Technol. Adv. Mater 11 (2010) 014101.
[139] V. Kandimalla, V. Tripathi, H. Ju, Crit. Rev. Anal. Chem 36 (2006) 73–106.
[140] M. Rendl, A. Bönisch, A. Mader, K. Schuh, O. Prucker, T. Brandstetter, et al., Langmuir 27 (2011) 6116–6123.
[141] F. Ricci, G. Palleschi, Biosens. Bioelectron 21 (2005) 389–407.
[142] X.-L. Luo, J.-J. Xu, Y. Du, H.-Y. Chen, Anal. Biochem 334 (2004) 284–289.
[143] D. Pradhan, Z. Su, S. Sindhwani, J.F. Honek, K.T. Leung, J. Phys. Chem. C 115 (2011) 18149–18156.
[144] L. Shi, Y. Xiao, I. Willner, Electrochem. Commun 6 (2004) 1057–1060.
[145] J. Wang, Chem. Rev 108 (2008) 814–825.
[146] K.E. Toghill, R.G. Compton, Int. J. Electrochem. Sci 5 (2010) 1246–1301.
[147] D. Ivnitski, B. Branch, P. Atanassov, C. Apblett, Electrochem. Commun 8 (2006) 1204–1210.
[148] W.H. Holzapfel, R. Geisen, U. Schillinger, Int. J. Food Microbiol 24 (1995) 343–362.
[149] Z. Ma, T. Ding, Nanoscale Res. Lett 4 (2009) 1236–1240.
[150] A. Wei, X.W. Sun, J.X. Wang, Y. Lei, X.P. Cai, C.M. Li, et al., Appl. Phys. Lett 89 (2006) 123902 (3pp).
[151] S. Bharathi, M. Nogami, Analyst 126 (2001) 1919–1922.
[152] A.L. Crumbliss, S.C. Perine, J. Stonehuerner, K.R. Tubergen, J. Zhao, R.W. Henkens, et al., Biotechnol. Bioeng 40 (1992) 483–490.
[153] S. Baek, P.S. Kutchukian, G.L. Verdine, R. Huber, T.A. Holak, K.W. Lee, et al., J. Am. Chem. Soc 134 (2012) 103–106.
[154] L. Sun, C.X. Wu, X.T. Zhou, Y.A. Zhang, T.L. Guo, Mater. Technol 30 (2015) 177–181.
[155] D. Guan, X. Gao, J. Li, C. Yuan, Appl. Surf. Sci 300 (2014) 165–170.
[156] J.-H. Jeun, K.-Y. Park, D.-H. Kim, W.-S. Kim, H.-C. Kim, B.-S. Lee, et al., Nanoscale 5 (2013) 8480–8483.
[157] J. Yu, Y. Wang, W. Xiao, J. Mater. Chem. A 1 (2013) 10727–10735.
[158] S. Gubbala, V. Chakrapani, V. Kumar, M.K. Sunkara, Adv. Funct. Mater 18 (2008) 2411–2418.
[159] A.N.M. Green, E. Palomares, S.A. Haque, J.M. Kroon, J.R. Durrant, J. Phys. Chem. B 109 (2005) 12525–12533.
[160] P. Docampo, P. Tiwana, N. Sakai, H. Miura, L. Herz, T. Murakami, et al., J. Phys. Chem. C 116 (2012) 22840–22846.
[161] H.J. Snaith, C. Ducati, Nano Lett 10 (2010) 1259–1265.
[162] T.P. Chou, Q. Zhang, G. Cao, M. Science, R. Hall, J. Phys. Chem. C 111 (2007) 18804–18811.
[163] M. Abd-ellah, S. Bazargan, J.P. Thomas, A. Rahman, S. Srivastava, X. Wang, et al., Adv. Electron. Mater 1 (2015) 1–6.
[164] S. Kumar, W. Ahlawat, R. Kumar, N. Dilbaghi, Biosens. Bioelectron 70 (2015) 498–503.
[165] M. Willander, K. Khun, Z.H. Ibupoto, Sensors 14 (2014) 8605–8632.
[166] N. Moghimi, F.R. Rahsepar, S. Srivastava, N. Heinig, K.T. Leung, J. Mater. Chem. C 2 (2014) 6370–6375.
[167] S. Bazargan, N.F. Heinig, J.F. Rios, K.T. Leung, J. Phys. Chem. C 116 (2012) 4979–4985.
[168] S. Bazargan, N.F. Heinig, D. Pradhan, K.T. Leung, Cryst. Growth Des 11 (2011) 247–255.
[169] G. Schmid, M. Bäumle, M. Geerkens, I. Heim, C. Osemann, T. Sawitowski, Chem. Soc. Rev 28 (1999) 179–185.
[170] G. Schmid, Adv. Eng. Mater 3 (2001) 737–743.
[171] L.S. Ott, R.G. Finke, Coord. Chem. Rev 251 (2007) 1075–1100.
[172] J.A. Enterkin, K.R. Poeppelmeier, L.D. Marks, Nano Lett 11 (2011) 993–997.
[173] U. Habibpour, V. Wang, Z.W. Palmer, R.E. Heiz, J. Appl. Sci 11 (2011) 1164–1170.
[174] J. Li, S. Guo, E. Wang, RSC Adv 2 (2012) 3579–3586.
[175] G.S. Aluri, A. Motayed, A.V. Davydov, V.P. Oleshko, K.A. Bertness, N.A. Sanford, et al., Nanotechnology 23 (2012) 175501–175512.
[176] C. Heiliger, M. Czerner, P.J. Klar, S. Hara, IEEE Trans. Magn 46 (2010) 1702–1704.
[177] H. Haberland, M. Karrais, M. Mall, Z. Phys. D – Atoms, Mol. Clust 20 (1991) 413–415.
[178] Y. Haberland, H. Mall, M. Moseler, M. Qiang, Y. Reiners, T. Thurner, J. Vac. Sci. Technol. A 12 (1994) 2925–2930.
[179] R.E. Palmer, S. Pratontep, H.G. Boyen, Nat. Mater 2 (2003) 443–448.
[180] M. Gracia-Pinilla, E. Martínez, G.S. Vidaurri, E. Pérez-Tijerina, Nanoscale Res. Lett 5 (2009) 180–188.
[181] S. In, A.H. Kean, A. Orlov, M.S. Tikhov, R.M. Lambert, Energy Environ. Sci 2 (2009) 1277–1279.
[182] A.I. Ayesh, N. Qamhieh, H. Ghamlouche, S. Thaker, M. El-Shaer, J. Appl. Phys 107 (2010) 034317 (5pp).
[183] S. Srivastava, J.P. Thomas, A. Rahman, M. Abd-ellah, M. Mohapatra, D. Pradhan, et al., ACS Nano 8 (2014) 11891–11898.
[184] M. Grätzel, Nature 414 (2001) 338–344.
[185] X. Wei, G. Zhu, J. Zhou, H. Sun, Mater. Chem. Phys 100 (2006) 481–485.
[186] L.B. Hong, B. Fultz, J. Appl. Phys 79 (1996) 3946–3955.
[187] Y. Dumpich, G. Wassermann, E.F. Manns, V. Keune, W. Murayama, S. Miyako, J. Magn. Magn. Mater 67 (1987) 55–64.
[188] Y. Sumiyama, K. Kadono, M. Nakamura, Trans. Japan Inst. Met 24 (1983) 190–194.
[189] L.H. Zhu, X.M. Ma, L. Zhao, J. Mater. Sci 36 (2001) 5571–5574.
[190] H. Wu, Y. Cao, P. Yuan, H. Xu, X. Wei, Chem. Phys. Lett 406 (2005) 148–153.
[191] M.V. Dozzi, E. Selli, J. Photochem. Photobiol. C 14 (2013) 13–28.
[192] Y.W. Heo, M.P. Ivill, K. Ip, S.J. Pearton, M.F. Chisholm, T. Steiner, Mater. Today (2004) 34–40.
[193] G. Korotcenkov, B.K. Cho, Sensors Actuators B 196 (2014) 80–98.
[194] S.B. Ogale, Adv. Mater 22 (2010) 3125–3155.
[195] J. Wallentin, M.T. Borgström, J. Mater. Res 26 (2011) 2142–2156.
[196] S. Pearton, Nanoscale 2 (2010) 1057–1068.
[197] S. Bazargan, K.T. Leung, J. Chem. Phys 137 (2012) 184704.
[198] M.G. Bawendi, M.L. Steigerwald, L.E. Brus, Annu. Rev. Phys. Chem 41 (1990) 477–496.
[199] A. Trinchi, K. Galatsis, W. Wlodarski, Y.X. Li, J. Am. Chem. Soc 349 (2014) 9250–9252.
[200] Y.S. Fu, X.W. Du, S.A. Kulinich, J.S. Qiu, W.J. Qin, R. Li, et al., J. Am. Chem. Soc 129 (2007) 16029–16033.
[201] A.B. Djurišić, Y.H. Leung, Small 2 (2006) 944–961.
[202] H. Search, C. Journals, A. Contact, M. Iopscience, I.P. Address, J. Phys. D Appl. Phys 11 (1978) 1543–1551.
[203] T. Matsuoka, T. Tohda, T. Nitta, J. Electrochem. Soc 130 (1983) 417–423.
[204] D. Wang, G. Xing, M. Gao, L. Yang, J. Yang, T. Wu, J. Phys. Chem 115 (2011) 22729–22735.
[205] P.P. Pal, J. Manam, Appl. Phys. A 116 (2014) 213–223.
[206] G.R. Li, C.R. Dawa, X.H. Lu, X.L. Yu, Y.X. Tong, Langmuir 25 (2009) 2378–2384.
[207] J.C. Sin, S.M. Lam, K.T. Lee, A.R. Mohamed, Ceram. Int 40 (2014) 5431–5440.
[208] J.-S. Kang, Y.-K. Jeong, J.-G. Kang, L. Zhao, Y. Sohn, D. Pradhan, et al., J. Phys. Chem. C 119 (2015) 2142–2147.
[209] L.N. Bai, S. Wang, H.M. Sun, Q. Jiang, J.S. Lian, Appl. Surf. Sci 313 (2014) 888–895.
[210] E. Ventosa, W. Xia, S. Klink, F. La Mantia, B. Mei, M. Muhler, et al., Chem. A Eur. J. 19 (2013) 14194–14199.
[211] A. Zhao, J. Masa, J. Energy Chem 23 (2014) 701–707.
[212] S.K.S. Patel, N.S. Gajbhiye, J. Magn. Magn. Mater 330 (2013) 21–24.
[213] Y. Chen, X.L. Xu, Phys. B Condens. Matter 406 (2011) 3121–3124.
[214] E. Millon, M. Nistor, C. Hebert, Y. Davila, J. Perrière, J. Mater. Chem 22 (2012) 12179–12185.
[215] J.N. Zeng, J.K. Low, Z.M. Ren, T. Liew, Y.F. Lu, Appl. Surf. Sci 198 (2002) 362–367.
[216] M.K. Nowotny, L.R. Sheppard, T. Bak, J. Nowotny, J. Phys. Chem. C 112 (2008) 5275–5300.
[217] A. Kubacka, M. Fern, G. Col, Chem. Rev 112 (2011) 1555–1614.
[218] G. Wang, H. Wang, Y. Ling, Y. Tang, X. Yang, R.C. Fitzmorris, et al., Nano Lett 11 (2011) 3026–3033.
[219] M.A. Rahman, S. Bazargan, S. Srivastava, X. Wang, M. Abd-Ellah, J.P. Thomas, et al., Energy Environ. Sci 8 (2015) 3363–3373.
[220] J. Su, X. Zou, J.-S. Chen, RSC Adv 4 (2014) 13979–13988.